Physical control of biological processes in the central equatorial Pacific Ocean

Marjorie A.M. Friedrichs*, Eileen E. Hofmann

Center for Coastal Physical Oceanography, Crittenton Hall, Old Dominion University, Norfolk, VA 23529, USA

Abstract

A five-component (phytoplankton, zooplankton, ammonium, nitrate, detritus) physical–biological model was developed to investigate the effects of physical processes on daily to interannual time scales, on the lower trophic levels of the central equatorial Pacific. Many of the biological processes included in the ecosystem model respond to environmental fluctuations with time scales between 1 and 10 d, which are not typically resolved by basin- to global-scale circulation models. Therefore, the equatorial Pacific ecosystem model is forced using daily information (solar radiation, velocity, temperature) from the Tropical Atmosphere Ocean (TAO) mooring array. The ecosystem model also requires vertical velocity information which necessitated the development of a method for computing daily vertical velocities from the TAO array. Much of the variability in primary production, plankton and nutrient concentrations observed in 1992 during the US Joint Global Ocean Flux Study Equatorial Pacific Process Study time-series cruises (TS1 and TS2), is well reproduced in the model simulations. Simulations demonstrate that lower primary productivities during TS1 as compared to TS2 result from the deeper thermocline that persisted during TS1 as a result of El Niño conditions; however, because of the simultaneous reduction in grazing pressure, simulated chlorophyll levels are similar for these two time periods. Simulations of this single-species ecosystem model successfully reproduce data collected both during and after the El Niño, suggesting that species composition changes are not of first-order importance when examining the effects of the 1991–92 El Niño on the equatorial Pacific ecosystem. A 60–70% increase in chlorophyll concentration and a 400% increase in the chlorophyll contribution by diatoms was associated with the passage of a tropical instability wave (20-d period) across the study site during TS2. This period of high chlorophyll concentration and diatom abundance coincided temporally with strong northward velocities and strong downwelling velocities in the upper euphotic zone. Observations and simulations suggest that this increase in chlorophyll concentration and change in species composition not only results from in situ diatom growth stimulated by increased iron concentrations, but also results from the advection of diatoms toward the convergent front located along the leading (western) edge of the instability wave. Equatorially trapped internal gravity waves can also stimulate in situ

---

* Corresponding author. Fax: + 1-757-683-5550.

E-mail address: marjy@ccpo.odu.edu (M.A.M. Friedrichs).

phytoplankton growth as high-frequency vertical motions introduce limiting micronutrients, such as iron, into the euphotic zone. Because iron can be taken up by the picoplankton on time scales much shorter than the wave period (6–8 days), these waves may provide a mechanism for effecting a large flux of iron into the euphotic zone. Exclusion of these high-frequency motions results in an iron flux to the euphotic zone that may be underestimated by more than 30%.

1. Introduction

Large areas of the open ocean are characterized by relatively low and stable phytoplankton biomass, which is typically dominated by small, rapidly growing pico- and nano-phytoplankton. Diatoms, which are larger and are often the dominant taxa associated with spring blooms in nutrient–rich coastal ecosystems, are generally absent. Within the subtropical gyres the phytoplankton community composition can be explained by the low levels of macronutrients (nitrate, phosphate); however, this explanation cannot hold for regions such as the central and eastern equatorial Pacific where nitrate and phosphate concentrations routinely exceed those required by phytoplankton (Barber, 1992).

Iron limitation and strong microzooplankton grazing were initially suggested as likely, but opposing, causes of such high-nutrient, low-chlorophyll (HNLC) conditions (Martin and Fitzwater, 1988; Martin et al., 1989; Banse, 1990; Martin et al., 1990). However, it is becoming increasingly clear that both factors are simultaneously required to explain many recent observations of plankton community dynamics in the central and eastern equatorial Pacific (Cullen et al., 1992; Frost and Franzen, 1992; Price et al., 1994; Landry et al., 1997). Iron is now known to enter this region primarily via upwelling from the Equatorial Undercurrent (Coale et al., 1996a). Typically iron is present in surface waters at concentrations low enough to hold local phytoplankton species below their physiological potential; however, half-saturation coefficients for iron uptake vary amongst species, with larger diatoms being held below their growth potential to a greater degree than the more dominant picoplankton (Price et al., 1994; Fitzwater et al., 1996; Zettler et al., 1996; Behrenfeld et al., 1996; Coale et al., 1996b). Microzooplankton rapidly graze the dominant small phytoplankton and can quickly respond to changes in phytoplankton abundance due to their high growth rates which may match or exceed those of their prey (Chavez et al., 1991; Landry et al., 1995; Coale et al., 1996b). Thus microzooplankton may also play a major role in controlling phytoplankton biomass.

One goal of the US Joint Global Ocean Flux Study (JGOFS) Equatorial Pacific process study (EqPac) was to examine why phytoplankton biomass and production remains low in the HNLC region of the central equatorial Pacific (Murray et al., 1992). As part of this study, four cruises were conducted during 1992: two survey cruises along 140°W (Fig. 1) (February/March (S1) and August/September (S2)) and two 20-d time-series cruises at 0°N, 140°W (March/April (TS1) and October (TS2)). Although EqPac was designed to examine seasonal time scales, the deeper thermocline and warmer surface water present in early 1992 (characteristic of El Niño conditions), dominated over the typical seasonal variability of this region, and thus unexpectedly allowed the

study of interannual effects (Murray, 1992). Much analysis has therefore been concentrated on comparing results from S1 and TS1, coinciding with the El Niño warm event, to those of S2 and TS2 which occurred during relatively cool surface water conditions. However, it is difficult to isolate the effect of an El Niño on an equatorial Pacific ecosystem since these events have interannual periodicities, whereas traditional biological observations such as those made during EqPac are taken on time scales of hours to days. Thus, many of the biogeochemical differences observed between these cruises are not necessarily attributable to the presence or absence of El Niño conditions, but rather may be due to higher frequency mesoscale events such as tropical instability waves or equatorially trapped internal gravity waves, which are known to be present in this region (Wunsch and Gill, 1976; Yoder et al., 1994; Lien et al., 1995; Flament et al., 1996).

An ecosystem model provides a framework for examining biological–physical interactions over a wide range of time scales by allowing individual biological responses to discrete physical processes to be isolated and quantified. Marine ecosystem models have only recently been applied to study lower trophic-level interactions in the equatorial Pacific. One of the first modeling studies (Chai et al., 1996) used an ecosystem model embedded within an ocean general circulation model to determine the nitrate budget for the equatorial Pacific Ocean on seasonal time scales. This model did not explicitly include iron limitation of primary production. However, the role of physiological limitation of phytoplankton photosynthesis on the maintenance of the HNLC condition was examined by performing modeling experiments in which photosynthetic parameters, such as the maximum specific growth rate and the initial slope of the *P–I* curve, were increased. Loukos et al. (1997) examined the effects of iron limitation on the plankton community at annual time scales, using a one-dimensional ecosystem model calibrated for $0°N$, $140°W$ and forced with vertically constant upwelling velocities. Model simulations demonstrated that in this region of the equatorial Pacific, it is not possible to reproduce observed variability in the rate of primary production using an ecosystem model in which nitrogen is specified to be the limiting nutrient.

A more complex nine-component ecosystem model containing multiple phytoplankton, zooplankton, and detritus size classes, and forced by an ocean general circulation model (Leonard et al., 1999) was run for five years in order to examine plankton variability on interannual time scales. This model focused on simulating general patterns occurring on the seasonal and interannual scales that were adequately resolved by the circulation model. Since many biological processes occur on relatively short (daily) time scales, an ecosystem model designed to reproduce EqPac observations must also resolve environmental fluctuations with time scales of 1–10 d. Therefore, in this analysis an ecosystem model for the plankton community at $0°N$, $140°W$ is developed which is directly forced with data from the Tropical Atmosphere Ocean (TAO) mooring array, rather than with circulation, light, and temperature fields obtained from theoretical models. Consequently, this model inherently includes physical processes and their associated temporal variability on multiple time scales.

In the following sections, relevant data sets are discussed and physical and biological components of the model are described. Model results, including those from a sensitivity analysis, are then examined and compared to data from the JGOFS EqPac cruises and the bio-optical mooring. These results are then discussed in the context of varying time scales, from interannual to mesoscale, to even higher frequency variability. A number of idealized modeling experiments are performed in order to determine specific ecological consequences resulting from environmental forcing mechanisms that occur over a wide range of time scales.
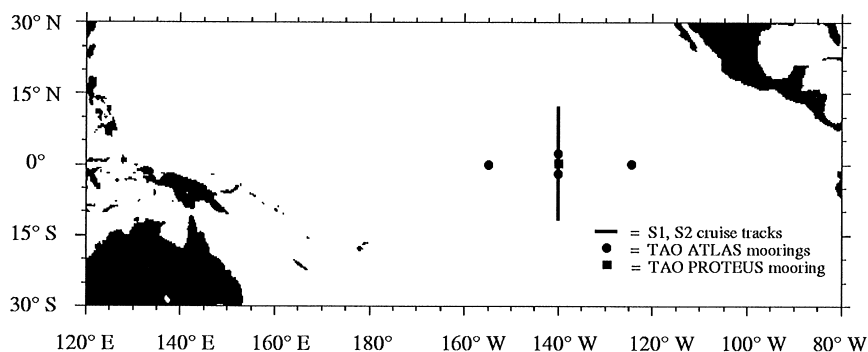
Fig. 1. Map showing locations of data sets used in this analysis: EqPac S1 and S2 cruises, four of the TAO ATLAS moorings, and a TAO PROTEUS mooring on which bio-optical instrumentation was also temporarily deployed. Note that TS1 and TS2 data are from a ship stationed at 0°N, 140°W.

2. Data

2.1. US JGOFS EqPac process study

The purpose of EqPac was to determine the fluxes of carbon and related elements, and the processes controlling those fluxes, between the euphotic zone and the atmosphere and deep ocean. Three issues of *Deep-Sea Research Part II* (Vol. 42, No. 2–3, 1995; Vol. 43, No. 4–6, 1996; Vol. 44, 9–10, 1997) are devoted to discussing the data and results obtained from this experiment, and synthesis papers will undoubtedly continue to appear in the literature for many years to come.

Although the 1992 EqPac experiment consisted of 13 separate cruises, the data used for this analysis are primarily from two process-oriented survey cruises along 140°W between 12°N and 12°S, S1 and S2, and two 20-d time-series cruises at 0°N, 140°W, TS1 and TS2 (Fig. 1). Details of these cruises are given in Murray et al. (1994, 1995). Nutrient, primary production, chlorophyll and zooplankton data were collected according to US JGOFS data protocols (http://usjgofs.whoi.edu/protocols.html), and were obtained for this study via the US JGOFS Data Management System, which is accessible through http://www1.whoi.edu/jgofs.html. Descriptions of these data can also be found in Barber et al. (1996) (primary production and phytoplankton chlorophyll), Landry et al. (1995), Roman et al. (1995), White et al. (1995) (zooplankton), McCarthy et al. (1996) (ammonium and nitrate), and Walsh et al. (1995) (euphotic zone depth).

Bio-optical sensors measuring light and fluorescence were also deployed on the 0°N, 140°W TAO mooring at 10, 25, 45, and 80 m (Foley et al., 1997). The surface instrument operated intermittently for about 400 d, whereas the deeper three sensors collected reliable data only during May–July 1992 (Foley et al., 1997). These data are also archived and available through the US JGOFS Data Management System (http://www.whoi.edu/jgofs.html).

2.2. Tropical Atmosphere Ocean moorings

In addition to the multidisciplinary data collected during the EqPac Process study, the TAO mooring array provides a suite of concurrent physical data (McPhaden et al., 1993, 1998), including
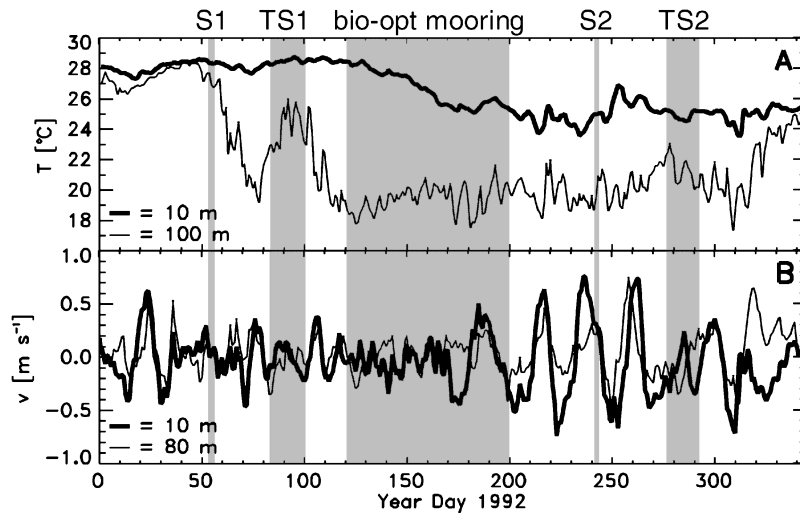
Fig. 2. (A) Temperature (10, 100 m) and (B) meridional velocity (10, 80 m) from TAO mooring at 0°N, 140°W. Shaded regions denote times of the JGOFS EqPac survey cruises (S1 and S2), time-series cruises (TS1 and TS2) and the time during which the bio-optical mooring was fully operational.

subsurface temperature time series (at 10 levels to 500 m depth) from ATLAS thermistor chain moorings (Hayes et al., 1991) located along the equator at 155°W, 140°W, and 125°W, and along 140°W at 2°N and 2°S (Fig. 1). A PROTEUS mooring located at 0°N, 140°W provides not only subsurface temperature time series, but also incoming solar radiation and subsurface velocity measurements (McPhaden et al., 1998). Data from these moorings are nearly continuous from September 1991 through the present, and are available via the TAO Home Page (http://www.pmel.noaa.gov/toga-tao).

The long-term time-series data available from the 0°N, 140°W TAO mooring (Fig. 2) are crucial for placing the four EqPac cruises in a physical context. During S1 the upper water column was unusually warm, with the thermocline extending to at least 100 m (Fig. 2A). These characteristics were typical of those observed throughout the 1991–92 El Niño. The following cruise (TS1) occurred during somewhat similar conditions, although by this time the temperature at 100 m had begun to drop: an indication of the waning of the El Niño. Conditions more typical of non-El Niño periods prevailed during the S2 and TS2 cruises, which were characterized by 25°C sea-surface temperatures and shallower thermocline depths.

Physical variability in the central equatorial Pacific is also present at much higher frequencies, as indicated by temperature oscillations of 2–4°C at 100 m, with periods of 6–8 d (Fig. 2A). These temperature oscillations result from high-frequency variability in the vertical velocity field, and are consistent with the period and latitudinal structure of equatorially trapped internal gravity waves (IGWs) of the first baroclinic vertical mode (Wunsch and Gill, 1976).

The meridional velocity time series (Fig. 2B) show variability in amplitude and direction that go from large ($>0.2\,\mathrm{m\,s^{-1}}$) positive (north) to large negative (south) with a period of 20 d. These features are tropical instability waves (TIWs). Since particle motions of these waves are described by eccentric ellipses oriented toward the north (Qiao and Weisberg, 1995), these waves are best
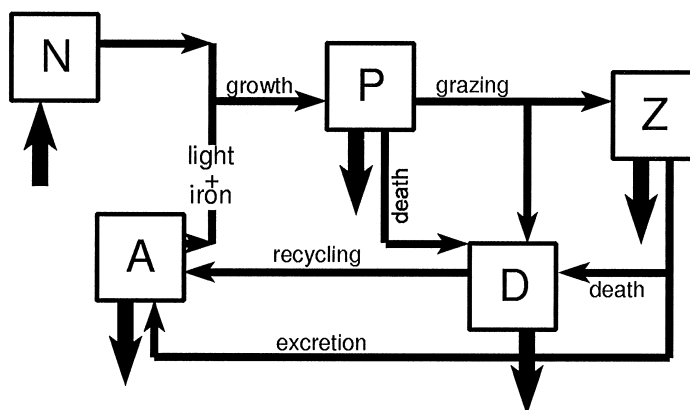
Fig. 3. Schematic of the five-component ecosystem model: phytoplankton (P), zooplankton (Z), ammonium (A), nitrate (N), and detritus (D). Large arrows represent the advection of model components into and out of the system; small arrows represent biological processes and transfers described in text.

observed via time series of meridional velocity. Zonal wavelengths range from 800 to 2000 km, and westward propagation occurs with phase velocities of roughly $0.6\,\mathrm{m\,s^{-1}}$ (Halpern et al., 1988; Perigaud, 1990; Qiao and Weisberg, 1995; Yu et al., 1995). These waves are also associated with regions of intense horizontal convergence, where dramatic concentrations of marine life have been observed (Yoder et al., 1994; Flament et al., 1996).

With the exception of the TIW on Year Day 25 of 1992 (YD25), these features did not appear in the meridional velocity time series until after YD170 (Fig. 2B), in accordance with previous observations that TIW activity is often suppressed under El Niño conditions (Legeckis, 1977). Six TIWs passed the 0°N, 140°W mooring after this time, the first of which occurred while the bio-optical mooring was in place. The TIW that coincided with S2 (YD240) was the largest in the time series, while that occurring during TS2 (YD285) was particularly small in amplitude.

3. Biological–physical model

The intent of this study is to examine first-order biological–physical interactions, and not to simulate all biological and physical processes of the equatorial Pacific. Therefore, a relatively simple five–component (phytoplankton (P), zooplankton (Z), ammonium (A), nitrate (N), and detritus (D)) ecosystem model is used (Fig. 3).

Each ecosystem component (C, expressed in terms of $\mathrm{mmol\,N\,m^{-3}}$) satisfies a general conservation equation of the form

$$\frac{\partial C(z,t)}{\partial t} = F_C(z,t) + B_C(z,t), \tag{1}$$

where F_C and B_C denote the physical and biological processes, respectively, which affect changes in the concentration of component C. In the equatorial Pacific many components of the ecosystem have vertical profiles that are nearly constant over time. Therefore, the model can be substantially

simplified by averaging over this vertical structure. Integrating over depth, (1) becomes

$$\frac{\partial \overline{C(t)}}{\partial t} = \overline{F_C(t)} + \overline{B_C}(t) - \frac{C(t)|_{(z=-E)}}{E(t)} \frac{d(-E(t))}{dt}, \tag{2}$$

where z is positive upwards. The depth of the base of the euphotic zone, $E(t)$, is computed daily as a function of the vertical attenuation coefficients, and is defined as the depth of the 0.1% light level. The overbar notation is reserved for quantities that are vertically averaged from the surface to $-E(t)$. (Unless otherwise specified, all vertical averages and integrations reported in this analysis are computed from the ocean surface to the base of the euphotic zone.) The last term on the right-hand side of Eq. (2) arises via Liebniz's rule, since the lower integral limit is a function of time.

3.1. Physical processes

3.1.1. Scale analyses

Scale analyses were used a priori to identify key dynamical processes which may have first-order effects on the various biological and chemical constituents of the model. In the equatorial Pacific region of interest for this study, vertical velocities are on the order of 10^{-4}–$10^{-5}\,\mathrm{m\,s^{-1}}$ (Bryden and Brady, 1985; see Appendix A) and vertical eddy diffusivities range between 10^{-3} and $10^{-5}\,\mathrm{m^2\,s^{-1}}$ (Carr et al., 1992), making vertical diffusion negligible compared to vertical advective processes (Carr et al., 1995). Similarly, horizontal diffusivities are on the order of 10^3–$10^4\,\mathrm{m^2\,s^{-1}}$ (Hansen and Swenson, 1996; Chai et al., 1996), while subsurface meridional and zonal velocities can reach 0.5 and $1\,\mathrm{m\,s^{-1}}$, respectively (McPhaden, 1993; Kessler and McPhaden, 1995), making horizontal diffusion negligible as compared to horizontal advection. These assumptions are consistent with both the data analysis of Carr et al. (1995) and the modeling work of Chai et al. (1996) at 140°W, which indicate that the turbulent diffusion of nitrate is typically an order of magnitude smaller than vertical nitrate advection. Thus F_C can be approximated as

$$\overline{F_C} = \frac{1}{E(t)} \int_{-E(t)}^0 \left(u\frac{\partial C}{\partial x} + v\frac{\partial C}{\partial y} + (w + w_C)\frac{\partial C}{\partial z} \right) dz, \tag{3}$$

where u, v, and w are the three components of velocity in the x (positive eastward), y (positive northward), and z (positive upward) dimensions respectively, and w_C is the vertical sinking rate of component C. At 140°W, $E(t)$ averages 120 m (Walsh et al., 1995). Zooplankton and detritus are assumed to sink with rates of $w_Z = 0.5\,\mathrm{m\,d^{-1}}$ and $w_D = 12\,\mathrm{m\,d^{-1}}$ respectively (Leonard et al., 1999); since the phytoplankton in this region are predominantly picoplankton, w_P is assumed to be negligible.

Scaling arguments can also be used to determine which terms in Eq. (3) are dominant for each of the five model components. Average estimates for the vertical and meridional advection of phytoplankton, zooplankton, nitrate, and ammonium are computed as a function of latitude by combining the S1 and S2 cruise data with average vertical profiles of meridional velocity (v) (from TAO data; mean from September 1, 1991 to September 1, 1995) and vertical velocity (w) (Bryden and Brady, 1985). The results demonstrate that near the equator, the ratio of meridional to vertical advection for phytoplankton and zooplankton is only 0.2–0.4, and nowhere within 4° of the equator for either the S1 or the S2 cruise does meridional advection ever exceed vertical advection
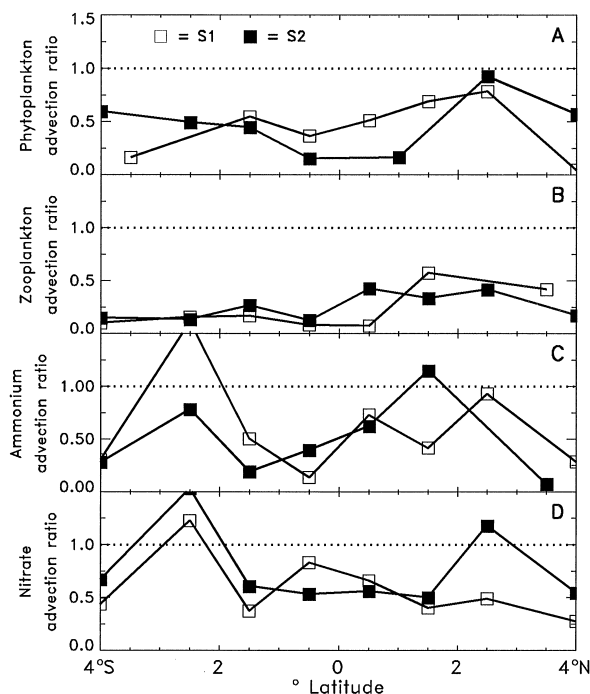
Fig. 4. Ratio of meridional to vertical advection for (A) phytoplankton chlorophyll (B) zooplankton, (C) ammonium, and (D) nitrate computed from S1 (□) and S2 (■) cruise data as a function of latitude.

Table 1
Comparison of the depth-averaged zonal advective terms computed from Zonal Flux cruise data (mean from 150–170°W), and vertical advective terms computed from S1 and S2 cruise data (mean from 3°N–3°S, 140°W), for four model components

	Zonal advection	Vertical advection (S1)	Vertical advection (S2)
P (mg chl m^{-3} d^{-1})	0.0011	0.0024	0.0044
Z (mmol C m^{-3} d^{-1})	0.01	0.12	0.19
A (mmol N m^{-3} d^{-1})	0.008	0.016	0.014
N (mmol N m^{-3} d^{-1})	0.07	0.10	0.16

(Figs. 4A and B). On the other hand, the ratio of meridional to vertical advection for ammonium and nitrate is 0.5–0.8 at the equator, and furthermore, within several degrees away from the equator meridional advection often exceeds vertical advection (Figs. 4C and D).

Zonal advection of the model components can be scaled using preliminary data from the Zonal Flux cruise (Le Borgne et al., 1999), carried out along the equator, from 165°E to 150°W in April–May 1996 (Table 1). Estimates of $\partial \bar{P}/\partial x$ and $\partial \bar{Z}/\partial x$ (Le Borgne et al., 1999, their Figs. 4b and d) and profiles of $\partial A/\partial x$ and $\partial N/\partial x$ (M. Rodier, personal communication) between 150°W and 170°W, were combined with a mean u profile computed from TAO data (September 1, 1991 to

September 1, 1995) at 140°W, in order to obtain estimates of zonal advection of each model component. (The fact that the gradients were computed 20° to the west of 140°W is not believed to significantly affect the results, since the zonal gradients appear to be relatively independent of longitude over these spatial distances.) Vertical advection is found to dominate zonal advection for both phytoplankton and zooplankton by factors of 3 and 16, respectively. However, zonal advection may be an important component in the nutrient balances: the ratio of vertical to zonal advection is between 1 and 2 for both nitrate and ammonium (Table 1).

This scale analysis thus shows that horizontal advection must remain as a first-order process in the nitrate balance, but can be neglected in the phytoplankton and zooplankton balances. Although negligible during the El Niño conditions of S1, horizontal advection may at times be an important component in the ammonium balance. Neglecting second-order terms, (3) becomes

$$\overline{F_P} = \frac{1}{E(t)} \int_{-E(t)}^{0} w \frac{\partial P}{\partial z} \, dz,$$

$$\overline{F_Z} = \frac{1}{E(t)} \int_{-E(t)}^{0} (w + w_Z) \frac{\partial Z}{\partial z} \, dz,$$

$$\overline{F_N} = \frac{1}{E(t)} \int_{-E(t)}^{0} \left(u \frac{\partial N}{\partial x} + v \frac{\partial N}{\partial y} + w \frac{\partial N}{\partial z} \right) dz,$$

$$\overline{F_A} = \frac{1}{E(t)} \int_{-E(t)}^{0} \left(u \frac{\partial A}{\partial x} + v \frac{\partial A}{\partial y} + w \frac{\partial A}{\partial z} \right) dz,$$

$$\overline{F_D} = \frac{1}{E(t)} \int_{-E(t)}^{0} (w + w_D) \frac{\partial D}{\partial z} \, dz. \tag{4}$$

3.1.2. Vertical advection

Estimates of vertical velocity (w) are required in order to compute vertical advection. A diagnostically computed w profile (constant in time) for the central equatorial Pacific (e.g. Bryden and Brady, 1985), or, alternatively, output from an ocean global circulation model (OGCM) (e.g. Harrison, 1996) could be used for this purpose. However, because a portion of this analysis is focused on biological responses to physical processes with time scales of days to weeks, a preferable approach is to estimate w directly from TAO data (u, v, T) at 140°W. The method used to estimate daily-varying vertical velocity as a function of depth is described in Appendix A. When averaged over four years (September 1, 1991 to September 1, 1995), these derived vertical velocities are typically only on the order of a few meters per day, with a maximum located near 70 m depth (Fig. 5). The standard deviations of these mean velocities ($(\langle w^2 \rangle / n)^{1/2}$) indicate a close agreement throughout most of the euphotic zone between these velocities and the diagnostic model results of Bryden and Brady (1985) (Fig. 5A). Although the mean vertical velocities are quite small (O(1–2 m d^{-1})), daily values of w may exceed 20 m d^{-1}, as is evident by the large standard deviations of the time series ($\langle w^2 \rangle^{1/2}$) (Fig. 5B). Instantaneous vertical velocities of this magnitude would be expected to have very significant effects on the biological community, and therefore cannot be neglected.
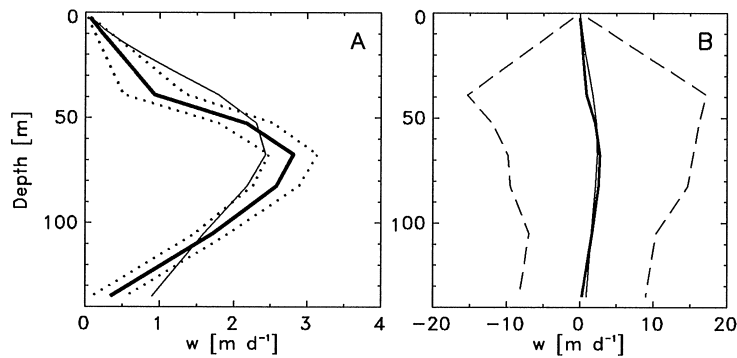
Fig. 5. Four-year mean (September 1, 1991–September 1, 1995) vertical velocity profile (thick solid line) obtained using the method described in Appendix A, along with the average vertical velocity profile of Bryden and Brady (1985) (thin solid line.) Superimposed are (A) the standard deviations of the means ($(\langle w^2 \rangle / n)^2$; dotted lines) and (B) the standard deviations of the time series ($\langle w^2 \rangle^{1/2}$; dashed lines). Note the different scales of the x-axes.

In order to estimate vertical advection, vertical gradients of each model component are also required. In this study, the vertical structure for phytoplankton, zooplankton, ammonium, and detritus is fixed. Since it does not evolve with time, it is important that this vertical structure be specified as accurately as possible. Data from the four JGOFS EqPac cruises show that the mean vertical structure of phytoplankton (Barber et al., 1996) and ammonium (McCarthy et al., 1996) can be described by a parabolic function with a concentration maximum (d_c) located at 45 m, as

$$C(z) = \frac{3\bar{C}}{E(2E - 3d_c)}[(d_c - E)^2 - (d_c + z)^2]. \tag{5}$$

In accordance with EqPac data (Roman et al., 1995), the model zooplankton decrease linearly with depth to a concentration of zero at $z = -E$:

$$Z(z) = 2\bar{Z}\left(1 + \frac{z}{E}\right). \tag{6}$$

Applying Eqs. (5) and (6) to estimates of $\bar{P}$, $\bar{A}$, and $\bar{Z}$ from TS2 yields the vertical profiles shown in Figs. 6A–C. On average, these functions fit the TS2 data (and data from the other EqPac cruises, not shown) quite well. The vertical distribution of the TS2 chlorophyll data is fit reasonably well by Eq. (5), but the parabolic relationship slightly underestimates chlorophyll at the surface and at the deep chlorophyll maximum (Fig. 6A). The TS2 ammonium observations are variable in the upper 75 m of the water column, but Eq. (5) provides a depth profile that is a reasonable fit to these data as well. The TS2 zooplankton data decrease linearly with depth; however, Eq. (6) overestimates biomass in the upper 20 m, and underestimates biomass in the lowest 20 m of the euphotic zone. Vertical profiles of nitrate are obtained by applying the Barber and Chavez (1991) $N:T$ regression to daily temperature values from the 140°W TAO mooring. Applying this regression to temperature data averaged over the TS2 time period yields a close fit between in situ nitrate measurements, and the modeled nitrate vertical structure (Fig. 6D). Comparisons between vertical structures obtained from Eqs. (5) and (6) and observations from the other EqPac cruises (not shown) are similar.
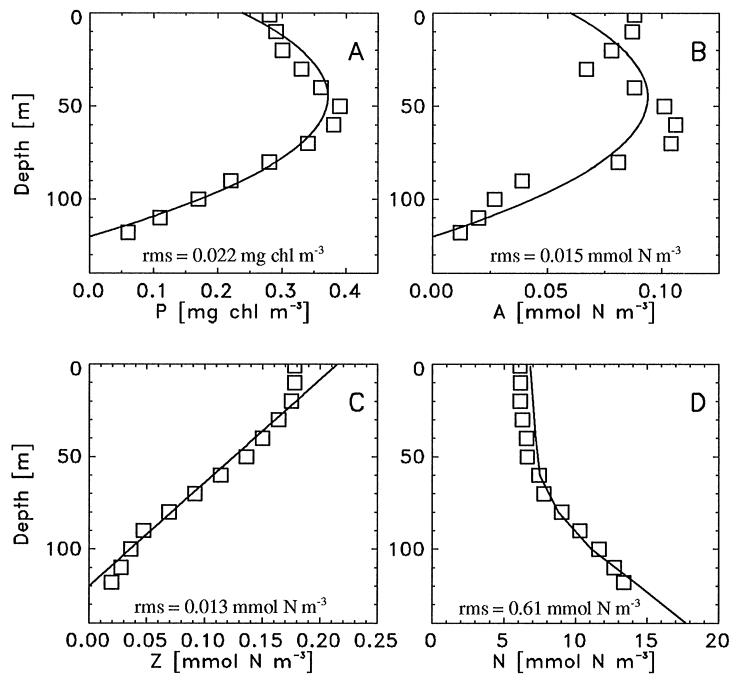
Fig. 6. Average vertical profiles (——) computed for the TS2 time period of (A) phytoplankton chlorophyll, (B) ammonium, (C) zooplankton, and (D) nitrate. Functional fits are described in text, and are based on the observed average euphotic zone depth (120 m), and average concentrations of phytoplankton (0.28 mg chl m^{-3}), ammonium (0.07 mmol N m^{-3}), and zooplankton (0.11 mmol N m^{-3}). Corresponding data averaged over the TS2 cruise (□), and root mean squared errors (rms) are indicated.

It is difficult to quantitatively estimate the vertical distribution of the detrital pool. However, because the sinking rate of detritus is an order of magnitude greater than local upwelling velocities, its concentration would be expected to increase with depth. For the purposes of this model, it is sufficient to assume that the detrital pool increases from a concentration of zero at the surface to a concentration of $2\bar{D}$ at $z = -E$:

$$D(z) = -\frac{2\bar{D}z}{E}. \tag{7}$$

Vertical advection is thus computed as the product of the daily-varying vertical gradient of each model component and the daily-varying vertical velocities of Appendix A. The resulting direct estimates of nitrate vertical advection averaged over 1992 and 1993 (10.5 and 12.8 mmol N m^{-2} d^{-1}, respectively) are similar to climatological modeling results (11.3 mmol N m^{-2} d^{-1}; Chai et al., 1996) (Table 2). Error bars on the direct estimates can be computed by substituting the average vertical velocity profile of Bryden and Brady (1985) for the daily-varying velocities; the results indicate that the direct estimates and modeled values are not significantly different.

Table 2
Vertically integrated (0–120 m) components of nitrate advection ($mmol\,N\,m^{-2}\,d^{-1}$). Direct estimates are computed from TAO mooring data, as described in text

Component of NO_3^- advection	1992 direct (this analysis)	1993 direct (this analysis)	Climatological model (Chai et al., 1996)
Vertical	10.5 ± 3.8	12.8 ± 2.1	11.3
Zonal	-7.7 ± 4.0	-7.9 ± 4.0	-5.3
Meridional	-1.9 ± 0.7	-2.3 ± 1.2	-1.6

3.1.3. Horizontal advection of nitrate and ammonium

Meridional gradients of nitrate are computed by applying an $N:T$ regression (Barber and Chavez, 1991) to temperature differences measured between the 2°N, 140°W and 2°S, 140°W TAO moorings; zonal gradients are similarly computed using temperature from 0°N, 125°W and 0°N, 155°W (Fig. 1). Because of the large distance between this latter pair of moorings, and since it would take 30 d for a particle traveling at an average velocity of $1\,m\,s^{-1}$ in the Equatorial Undercurrent to traverse this distance, the $N:T$ regressions are applied to temperatures averaged over 30 d. The product of these zonal (meridional) gradient estimates and daily zonal (meridional) velocity measurements from the TAO mooring at 140°W yields direct estimates of the zonal (meridional) advection of nitrate. Resulting zonal (meridional) estimates averaged individually over 1992 and 1993 are -7.7 and $-7.9\,mmol\,N\,m^{-2}\,d^{-1}$ (-1.9 and $-2.3\,mmol\,N\,m^{-2}\,d^{-1}$) respectively (Table 2).

Errors in these horizontal nitrate fluxes are estimated by computing temperature gradients via upstream and downstream differences, as opposed to the centered difference approach described above. The larger error associated with the zonal advection term ($4\,mmol\,N\,m^{-2}\,d^{-1}$) as compared to that associated with the meridional advection term ($2\,mmol\,N\,m^{-2}\,d^{-1}$) is a manifestation of the greater spacing between the zonal moorings. Although the meridional gradients are computed over much smaller distances, the upwelling-induced temperature minimum between 2°N and 2°S may cause errors in this estimate as well (Kessler and McPhaden, 1995). Nevertheless, the direct estimates of horizontal nitrate advection averaged over 1992 and 1993 are not significantly different from independent modeling results (Chai et al., 1996) (Table 2).

The previous scale analysis demonstrated that for non-El Niño conditions, horizontal advection may be a first-order term in the ammonium balance. Unfortunately, an ammonium:temperature relationship, analogous to the one for $N:T$ described above, does not exist and therefore it is not possible to create a daily time series of the horizontal advection of ammonium. Consequently, these terms are set to zero, and the errors resulting from this approximation will be examined in the following section.

3.1.4. Light

The biological model is forced by incoming solar radiation, specifically the photosynthetically active portion of the visible light spectrum (PAR). The value of PAR at the ocean surface (I_s) is a function of the hour of day (τ), clear sky value (I_0), and fraction cloud cover (C_s), and can be

computed as

$$I_s = I_0(1 - C_s)\sin(2\pi(\tau - 0.25)). \tag{8}$$

In this formulation τ represents non-dimensionalized time ($\tau = t/(24\,h)$, where $t = [0,24\,h]$). An atmospheric model (Gregg and Carder, 1990) is used to compute daily estimates of I_0. The fraction of cloud cover is obtained by comparing incident radiation measurements from the TAO 140°W mooring with the corresponding output from a clear–sky irradiance model (Frouin et al., 1989).

3.2. Biological processes

The various pathways for nitrogen cycling in the model ecosystem (Fig. 3) are described by the following equations:

$$\overline{B_P} = \overline{PP}(Fe, I, \bar{P}) - \bar{G}(\bar{P}, \bar{Z}) - \phi_P P$$

$$\overline{B_Z} = \gamma \bar{G}(\bar{P}, \bar{Z}) - \phi_Z \bar{Z},$$

$$\overline{B_N} = -\overline{NP}(Fe, I, \bar{P}, \bar{A}),$$

$$\overline{B_A} = -\overline{RP}(Fe, I, \bar{P}, \bar{A}) + \beta \phi_Z \bar{Z} + r_D \bar{D},$$

$$\overline{B_D} = \phi_P \bar{P} + (1 - \beta)\phi_Z \bar{Z} + (1 - \gamma)\bar{G}(\bar{P}, \bar{Z}) - r_D \bar{D}. \tag{9}$$

The biological processes affecting phytoplankton biomass are primary production $\overline{PP}$, grazing by zooplankton ($\bar{G}$), and natural mortality ($\phi_P \bar{P}$), where ϕ_P (d^{-1}) represents a linear loss rate. A fraction (β) of the grazed phytoplankton is assumed to represent zooplankton growth from assimilated ingestion. This growth is partially offset by a generalized loss term ($\phi_Z \bar{Z}$), where ϕ_Z (d^{-1}) is a linear loss rate. A fraction (β) of this term represents zooplankton excretion, and the remainder is attributed to losses such as natural mortality and predation. Primary production is supported by both nitrate uptake (new production; $\overline{NP}$) and ammonium uptake (regenerated production; $\overline{RP}$). Other biological processes affecting the ammonium balance include zooplankton excretion and recycling via the detrital pool ($r_D \bar{D}$), where r_D represents a generalized rate at which detritus is recycled into ammonium. Biological processes affecting the detrital pool include contributions from phytoplankton and zooplankton mortality, unassimilated grazing, and the loss of detrital nitrogen to ammonium nitrogen via recycling. As formulated above, the model requires specific parameterizations for grazing, primary production, regenerated production, and new production as discussed in the following sections. Parameter values and descriptions are given in Table 3.

3.2.1. Grazing

Following the approach described by Franks et al. (1986), zooplankton grazing is assumed to be given by

$$\bar{G}(\bar{P}, \bar{Z}) = g\bar{P}Z\Lambda(1 - e^{-P\Lambda}). \tag{10}$$

This modified form of Ivlev's (1955) grazing formulation accounts for food-acclimatized grazing and has been found to stabilize model output by reducing unrealistic P/Z oscillations. The Ivlev

Table 3
Values, units, and definitions of the parameters used in the biological model

	Value	Units	Definition
w_Z	0.5	$m\,d^{-1}$	Zooplankton sinking rate
w_D	12	$m\,d^{-1}$	Detrital sinking rate
ϕ_P	0.45	d^{-1}	Phytoplankton loss rate
ϕ_Z	0.75	d^{-1}	Zooplankton loss rate
γ	0.75	none	Zooplankton assimilation efficiency
β	0.3	none	Ammonium regeneration fraction
r_D	1.0	d^{-1}	Detrital regeneration rate
g	29	d^{-1}	Zooplankton maximum grazing rate
Λ	1.0	$(mmol\,N\,m^{-3})^{-1}$	Ivlev grazing parameter
k_{Fe}	0.034	$\mu mol\,Fe\,m^{-3}$	Iron half-saturation value
α	29	$d^{-1}(E\,m^{-2}\,h^{-1})^{-1}$	Initial slope of $P-I$ curve
P_M	14	d^{-1}	Maximal rate of photosynthesis
k_A	0.1	$mmol\,N\,m^{-3}$	Ammonium half-saturation value
d_c	45	m	Depth of maximum P, A concentration
Fe_{min}	0.026	$\mu mol\,Fe\,m^{-3}$	Minimum concentration of iron
m_{Fe}	0.001	$\mu mol\,Fe\,m^{-4}$	Slope of iron profile

constant, Λ, is assumed to fall between 0.1 and 2.0 $(mmol\,N\,m^{-3})^{-1}$ (Franks et al., 1986). A value for the maximal grazing rate, g, is determined such that in situ specific daily grazing rates, defined as $\bar{G}/\bar{P}$, predicted by the model agree with those observed during the EqPac experiment (Murray et al., 1994; Landry et al., 1997).

3.2.2. Primary production

Because recent results of in situ iron additions to macronutrient-rich equatorial waters during the IronEx cruises have unequivocally established that the availability of iron limits the cell division rates and abundance of phytoplankton (Frost, 1996; Behrenfeld et al., 1996), iron limitation is assumed a priori. Thus, instead of *re–testing* the iron hypothesis, the novel approach of *assuming* iron limitation and examining the implications for marine ecosystem structure at 0°N, 140°W is taken. Until more information becomes available on iron chemistry and the specific roles various forms of iron play in equatorial ecosystems, an explicit iron model cannot be justified. Therefore, in this study iron concentration is not included as a separate model component, but rather it is included in the growth term where iron limitation is specified.

In situ data from the bio-optical mooring indicate that equatorial Pacific phytoplankton populations are light limited, and quickly respond to variations in incoming radiation, such as those due to changing cloud cover (Foley et al., 1997). Thus, a multiplicative approach was chosen for the primary production model, allowing both iron and light to simultaneously limit growth. From these considerations, daily depth-averaged gross primary production can be represented by

$$\overline{PP} = \frac{1}{E}\int_{-E}^{0} Q_{Fe}\,P(z)\int_{0}^{1} Q_I\,d\tau\,dz, \tag{11}$$

where Q_{Fe} represents the functional dependence of primary production on iron concentration and Q_I represents the dependence on incoming PAR. Since time scales of primary interest range from a week to a year, Q_I is integrated over t, in order to filter out changes in phytoplankton growth that occur on time scales less than a day.

Iron limitation of phytoplankton growth is assumed to follow Michaelis–Menten kinetics:

$$Q_{Fe} = \frac{Fe}{Fe + k_{Fe}}, \tag{12}$$

where Fe is the iron concentration, and $k_{Fe} = 0.034 \, \mu\text{mol Fe m}^{-3}$ (Price et al., 1991) is taken to be the half-saturation coefficient for iron uptake by the ambient picoplankton community. Due to the difficulties inherent in measuring in situ iron concentrations, relatively few data are available. Therefore, an iron–temperature relationship was determined from data collected below the euphotic zone between $\pm 2°$ of the equator at 140°W (Leonard et al., 1999). Data from both the JGOFS EqPac cruises as well as the July 1990 Feline cruise along 140°W (Gordon et al., 1997) were used to compute

$$Fe[\mu\text{mol Fe m}^{-3}] = 1.028 \, (0.499 - 0.019 T[°\text{C}]). \tag{13}$$

This relationship is valid only in waters where iron is not limiting, and therefore must only be applied near the base of the euphotic zone. In this analysis it is applied only to the subsurface (100 m) TAO temperature data at 140°W.

A bilinear approximation to the empirical relationship for iron concentration as a function of depth (Gordon et al., 1997) can be expressed as $Fe(z) = \text{MAX}[Fe_{min}, Fe(z = -100) - m_{Fe}(z + 100)]$, where m_{Fe} is the slope of the linear profile, and Fe_{min} is the minimum iron concentration which may result partially from atmospheric deposition (Duce and Tindale, 1991) and/or iron recycling (Landry et al., 1997). Following Gordon et al. (1997), Fe_{min} is taken to be $0.026 \, \mu\text{mol Fe m}^{-3}$, i.e. slightly less than the current instrumental detection limit of $0.03 \, \mu\text{mol Fe m}^{-3}$, and m_{Fe} is $0.001 \, \mu\text{mol Fe m}^{-4}$. When combined with the temperature-derived iron concentrations at 100 m, this formulation yields a daily-varying vertical profile of iron concentration, and has a distinct advantage over other related studies (Landry et al., 1997; Loukos et al., 1997; Leonard et al., 1999) which are very sensitive to the poorly known and widely varying carbon-to-iron ratios (Gordon et al., 1997).

The functional dependence of primary production on light is modeled using an adaptation of the relationship given in Platt et al. (1980):

$$Q_I = P_{max}(1 - e^{-I\alpha/P_{max}}), \tag{14a}$$

where I is the irradiance (PAR), P_{max} is the maximum (nutrient-saturated) rate of photosynthesis in the absence of photoinhibition, and α is the initial slope of the P–I curve. Recent experimental evidence (Cullen et al., 1992) has indicated that in the central equatorial Pacific α is roughly constant throughout daylight hours, whereas P_{max} undergoes diel variations with the highest values corresponding to times of highest incident radiation. Thus P_{max} was assumed to vary sinusoidally between 0 and P_M:

$$P_{max}(\tau) = P_M \sin(2\pi(\tau - 0.25)). \tag{14b}$$

Estimates of P_M and α can be derived from data presented in Cullen et al. (1992); however, their corresponding parameters were obtained under ambient nutrient conditions, whereas P_M and α are defined for iron-saturated conditions. Therefore, to obtain true estimates of nutrient-saturated photosynthetic parameters, the values of Cullen et al. (1992) ($P_{max}^{ambient} = 4.5\,\text{mg C mg chl}^{-1}\,\text{h}^{-1}$ and $\alpha^{ambient} = 9.2\,\text{mg C mg chl}^{-1}\,\text{h}^{-1}\,(\text{E m}^{-2}\,\text{h}^{-1})^{-1}$) must be divided by the limiting factor, Q_{Fe}. For an iron concentration of 0.005–$0.025\,\mu\text{mol Fe m}^{-3}$, below the level of instrumental detection (Gordon et al., 1997), and a carbon:chlorophyll ratio of 40–$100\,\text{mg C mg chl}^{-1}$ (Chavez et al., 1996), P_M is in the range 3–$21\,\text{d}^{-1}$, and $\alpha = 5$–$42\,\text{d}^{-1}\,(\text{E m}^{-2}\,\text{h}^{-1})^{-1}$. These ranges are also consistent with values estimated from more recent JGOFS EqPac data (Lindley et al., 1995).

PAR at a given time and depth is determined by the incident surface value (I_s), and the depth-dependent attenuation, $R(z)$:

$$I(\tau, z) = I_s(\tau)R(z).\tag{15}$$

Many types of models exist for describing the attenuation of PAR with depth. These range from the very simple bulk exponential formulations frequently used in ecosystem models (e.g. Steele and Frost, 1977; Hofmann and Ambler, 1988), to the complex spectral models in which the photosynthetic spectrum may be split into as many as 61 wavebands (e.g. Morel, 1988). In this region where light limitation is typically of secondary importance to iron limitation, a complex spectral model is not justified; however, a higher degree of resolution than that afforded by assuming a constant attenuation with depth is warranted. Therefore, self-shading by phytoplankton, as described by Anderson (1993), was included (Appendix B). Daily estimates of euphotic zone depth (E; defined as the depth at which I is attenuated to 0.1% of its surface value, I_s) can then be obtained by solving $R(z) = 0.001$ for z.

Substituting Eqs. (14a), (14b) and (15) into Eq. (11) and performing the time integral analytically yields

$$\overline{PP} = \frac{P_M}{E\pi}\int_{-E}^{0} Q_{Fe}(1 - \exp[-I_0(1 - C_s)R(z)\alpha/P_M])P(z)\,dz.\tag{16}$$

The depth integration of (16) is computed at each model time interval.

Net primary production, defined as the difference between gross primary production and respiration ($\overline{NPP} = \overline{PP} - r\bar{P}$), was used as a diagnostic quantity to determine the degree of agreement between simulated and observed phytoplankton distributions. For this calculation, $r = 0.28\,\text{d}^{-1}$, which is an average specific phytoplankton respiration rate that is consistent with values reported for this region of the equatorial Pacific (Murray et al., 1994; Coale et al., 1996)

3.2.3. Regenerated production

Recent experimental evidence has revealed that in the equatorial Pacific, ammonium is typically given preference over nitrate as a source of nitrogen to fuel primary production. For instance, McCarthy et al. (1996) observed a strong suppressing effect of ammonium on nitrate uptake rates, with mean values for ammonium uptake rates being 8 times greater than those for nitrate during both S1 and S2. Therefore, if ammonium concentrations are high enough to provide enough

nitrogen to fuel all primary production, that is, if

$$\mu_{max} \frac{A}{k_A + A} > \mu,$$ (17)

where μ is defined as the depth-averaged phytoplankton growth rate ($\mu = \overline{PP}/\overline{P}$) and μ_{max} is defined to be the iron-saturated growth rate (obtained using the solution of (16) for $Q_{Fe} = 1$), then regenerated phytoplankton production equals primary production, $\overline{RP} = \overline{PP}$. On the contrary, if there is not adequate ammonium, i.e. if (17) is not satisfied, then

$$\overline{RP} = \mu_{max} \frac{A}{k_A + A} \overline{P}.$$ (18)

This formulation (Hurtt and Armstrong, 1999) results in ammonium uptake exceeding nitrate uptake by a factor of 7, which is in close agreement with observations of McCarthy et al. (1996).

3.2.4. New production

New production ($\overline{NP}$) is defined as that portion of total primary production that is supported by nitrate uptake, instead of by ammonium utilization. Thus, new production can be computed simply as

$$\overline{NP} = \overline{PP} - \overline{RP}.$$ (19)

The above formulations for new and regenerated production are consistent with recent observations (Timmermans et al., 1994) that although nitrate reductase activity, and hence total primary productivity, is explicitly dependent on the degree of iron limitation, regenerated production is *not* directly influenced by the absence or presence of iron. Finally, the traditional definition of the f-ratio (Dugdale and Goering, 1967), $f = \overline{NP}/\overline{PP}$, is used as a diagnostic quantity to compare model-derived results to values of the f-ratio determined experimentally.

3.3. Model implementation

The five-component model equations were solved using an explicit second-order Runge–Kutta scheme, with a time step of one day. The model parameter values (Table 3) were chosen to be consistent with the sources cited above. The initial depth-integrated nitrate concentration was estimated by applying the $N:T$ relationship to 31 d (August 1–31, 1991) of subsurface TAO temperature data at 140°W and performing the corresponding depth integral: $\overline{N}(t = 0) = 8.7 \, \text{mmol N m}^{-3}$. Using mean values for the forcing functions, the model was then run until steady-state values were obtained for each model component: $\overline{P} = 0.20 \, \text{mmol N m}^{-3}$, $\overline{Z} = 0.10 \, \text{mmol N m}^{-3}$, $\overline{A} = 0.07 \, \text{mmol N m}^{-3}$, $\overline{D} = 0.13 \, \text{mmol N m}^{-3}$. Using these values as initial conditions and the daily-varying forcing functions, the model was then run from September 1, 1991 to September 1, 1992 to obtain a reference simulation. This simulation then provides a baseline for comparison with results from other simulations in which parameters and forcing functions are modified.

4. Results

4.1. Parameter sensitivity analysis

Although the model requires the specification of 16 parameters, the results are significantly dependent on only a subset of those listed in Table 3. In order to determine which parameters are most critical in this analysis, a sensitivity analysis was performed. It is computationally intensive to vary each model parameter independently over the entire parameter space. Much can be learned by simply increasing and decreasing each parameter, and then examining the resultant effect on various model components and diagnostics.

In this study, each parameter was increased by 25% (decreasing by 25 or 50% yields similar results), the model was run using average, steady forcing until P reached steady state (less than 30 d), and the effect on P, Z, A, N, and PP was examined. Following Fasham et al. (1993), the effect of a given parameter, k, was quantified by calculating a normalized sensitivity, $S_C(k)$, defined as

$$S_C(k) = \frac{\dfrac{C(k) - C_s}{C_s}}{\dfrac{k - k_s}{K_s}}, \tag{20}$$

where C_s is the value of a model component for the reference case with the parameter value k_s, and $C(k)$ is the value for the case when the parameter has the adjusted value k. Thus S_C is a measure of the fractional change in the model component C compared to a fractional change in the parameter of interest (Table 4).

Some of the sensitivity results given in Table 4 are contrary to what might be expected for an iron-limited ecosystem. For instance, phytoplankton depends not on the growth parameters (e.g. P_M, α, k_{Fe}), nor the iron concentration in the euphotic zone (Fe_{min}, m_{Fe}), nor the phytoplankton death rate (ϕ_P); S_P values for all these parameters are less than 0.1. Rather, phytoplankton depends on the grazing parameters (g, Λ, γ) and the zooplankton mortality rate (ϕ_Z) as shown by the higher S_P values for these parameters, ranging from 0.4 to 0.8. This is indicative of an ecosystem under top-down control (Klein and Steele, 1985); despite iron limitation, the phytoplankton population is strongly controlled by its predators, the zooplankton. Zooplankton biomass, on the other hand, is more sensitive to phytoplankton growth parameters ($S_Z = 0.8$–1.0) than to grazing parameters ($S_Z = 0.3$–0.7), further demonstrating the tight coupling between P and Z. Thus, if the phytoplankton specific growth rate is increased by means of an enrichment in available iron supply, a larger response in zooplankton than phytoplankton might be expected; this possibility will be discussed further in the following section.

The concentration of ammonium is strongly dependent on the choice of both iron and ammonium half-saturation coefficients ($S_A = -0.7$ for k_{Fe} and $S_A = 1.0$ for k_A). On the contrary, nitrate concentration is not strongly dependent on any of the model parameters listed in Table 4 ($/S_N/ < 0.5$ for all 16 model parameters); instead, it depends primarily on the physical advection of nitrate into the system. In fact, if ammonium concentrations are high enough to fuel all primary production, i.e. (17) is satisfied, then $B_N = 0$ and N is independent of the other model components (Klein and Steele, 1985).

Table 4
Results of analysis of model sensitivity to changes in model parameters. Each parameter was increased and decreased by 25%. The resulting average fractional change in four model components and primary production as computed from Eq. (20) $(S_P, S_Z, S_A, S_N, S_{PP})$ is given. Dashes indicate model insensitivity ($|S_c| < 0.15$) to parameter changes

|	S_P	S_Z	S_A	S_N	S_{PP}
G	− 0.4	− 0.3	---	− 0.3	− 0.4
Λ	− 0.8	− 0.5	0.2	− 0.5	− 0.7
ϕ_Z	0.5	− 0.6	---	0.3	0.4
γ	− 0.4	0.7	---	− 0.3	− 0.4
k_{Fe}	---	− 0.9	− 0.7	---	− 0.5
Fe_{min}	---	0.7	0.6	---	0.3
m_{Fe}	---	− 0.3	− 0.2	---	---
P_M	---	1.0	---	---	0.5
α	---	0.8	---	---	0.4
d_c	---	− 0.6	---	---	− 0.3
ϕ_P	---	− 1.0	---	---	---
k_A	---	---	1.0	---	---
r_D	---	---	0.2	---	---
w_D	---	---	− 0.2	---	---
w_Z	---	---	---	---	---
β	---	---	---	---	---

4.2. Reference simulation

4.2.1. Physical forcing fields w and Fe

The physical fields used to force the reference simulation exhibit variability over a wide range of time scales. In order to isolate the variability caused by TIWs from that of the IGWs, time series of vertical velocity and iron concentration are 7-d low-pass filtered (Figs. 7A–F) and 12-d high-pass filtered (Figs. 7G–I). (Note that the *x*-axes in Fig. 7 extend over differing lengths of time and dates, in order to highlight the specific frequencies of interest.)

Despite the El Niño conditions present in early 1992, this time period is characterized by intervals of strong upwelling and downwelling with vertical velocities exceeding $20\,\mathrm{m\,d^{-1}}$ (thick lines; Figs. 7A and B). Clearly, the presence of El Niño conditions in early 1992 does not necessarily result in weak vertical velocities. However, the deeper thermocline present during this time period (Fig. 2) causes upwelling to be less effective at bringing high iron water to the surface and therefore iron concentrations remain low through YD60 (Fig. 7C).

Tropical instability waves are responsible for a large portion of the variability apparent in Figs. 7A–C. These 20-d oscillations dominate the time series of meridional and vertical velocity in the latter half of 1992. A closer inspection of these waves reveals that northward velocities ($v > 0$) are associated with downwelling ($w < 0$), while upwelling ($w > 0$) is associated with southward velocities ($v < 0$; Figs. 7D and E). Iron concentrations at 80 m also exhibit a 20-d periodicity, but these concentrations have a phase lag of $90°$ with respect to vertical velocity (Fig. 7F). Because iron concentrations increase with depth, periods of upwelling ($w > 0$) are associated with increasing iron
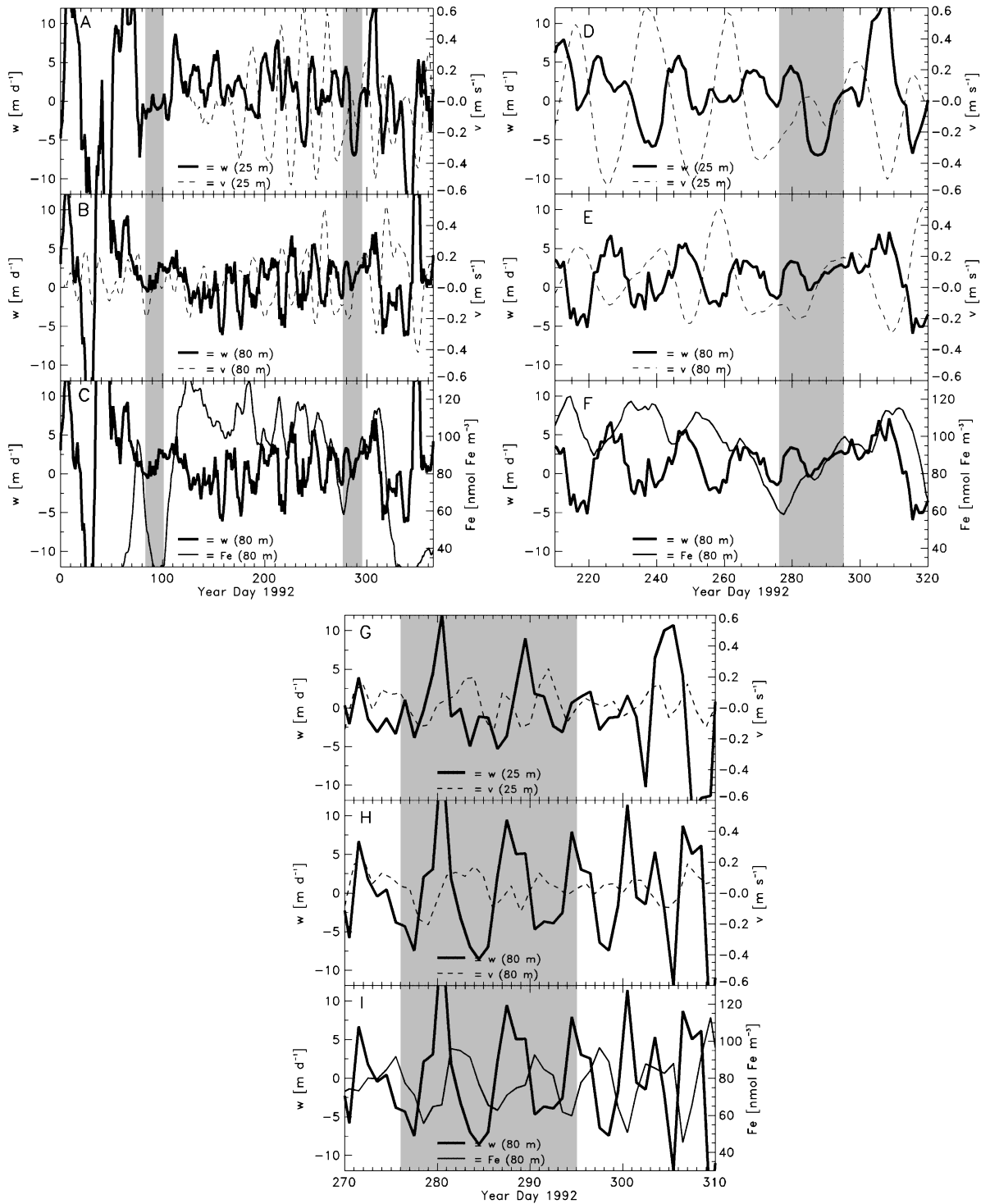
concentrations ($\partial Fe/\partial t > 0$), whereas periods of downwelling ($w < 0$) are associated with decreasing iron concentrations ($\partial Fe/\partial t < 0$).

Higher frequency variability corresponding to equatorially trapped internal gravity waves also exists. This variability is particularly visible if the lower frequency motions are removed with a 12-d high-pass filter, and the time axis is expanded (Fig. 7G–I). Between YD270 and YD310, for example, 6–7 oscillations of vertical velocity and iron concentration are observed, with two large upwelling events occurring during the TS2 cruise (Fig. 7C). Again, iron concentration is highly correlated with vertical velocity, with iron concentration lagging vertical velocity by 90°, i.e. iron increases during periods of upwelling.

4.2.2. Simulated time series

Using unfiltered time series of the forcing fields, simulated time distributions of primary production, phytoplankton chlorophyll, zooplankton biomass, ammonium, and nitrate were obtained (Fig. 8). (Throughout this paper, constant ratios of $C:\mathrm{chl} = 70\,\mathrm{mg\,C\,(mg\,chl)}^{-1}$ and $C:N = 6.6\,\mathrm{mmol\,C\,(mmol\,N)}^{-1}$ are used to convert phytoplankton in terms of $\mathrm{mmol\,N\,m}^{-3}$, as computed in the model, to phytoplankton in terms of the more meaningful unit: $\mathrm{mg\,chl\,m}^{-3}$.) These distributions show a wide range of temporal variability including the strong 6–8-d periodicity observed in the vertical velocity and iron concentration forcing fields (Figs. 7I). For example, over the time period during which the bio-optical mooring was fully operational, 11–13 such oscillations are evident in primary production, phytoplankton, zooplankton, ammonium, and nitrate (Fig. 8). Hence, the higher frequency motions observed in the environment are reflected in the simulated biological distributions.

Variability also exists on annual/interannual time scales. The average rate of primary production prior to YD100 is nearly 40% lower than that estimated for the time period spanning YD100-YD300. Similarly, the average rate of primary production between YD320 and YD420 is 30% lower. These time periods are associated not only with a decrease in mean value, but also with a dampening of high-frequency variability. Time series of zooplankton biomass, ammonium concentration, and nitrate concentration (Figs. 8C–E) exhibit similar trends; however, this is not the case for phytoplankton chlorophyll (Fig. 8B). The mean value and variability in the phytoplankton time series remain nearly constant throughout the simulation: no interannual variability is observed.

The net upward trend in nitrate concentration throughout the simulation is an artifact that results from an inability to compute the horizontal component of ammonium advection. Because ammonium is the preferred nitrogen source for the simulated phytoplankton, the lack of this significant advective loss term in the ammonium balance causes the phytoplankton to take up too much ammonium in place of nitrate, resulting in artificially high nitrate concentrations. If horizontal ammonium advection is assumed to be constant and equal to $0.015\,\mathrm{mmol\,N\,m}^{-3}\,\mathrm{d}^{-1}$, a reasonable assumption based on Fig. 4 and Table 1, this drift is nearly eliminated (Fig. 8E), with no substantial effect on any other model components.

Fig. 7. Low-pass filtered (A–F) and high-pass filtered (G–I) time series of derived vertical velocity at 25 and 80 m, measured TAO meridional velocity at 25 and 80 m, and derived iron concentration at 80 m. Shaded regions denote times of the JGOFS EqPac cruises. Scales and dates on the x-axes are varied in order to highlight different scales of variability: (A–C) interannual (El Niño), (D–F) monthly (TIW), and (G–I) weekly (IGW).
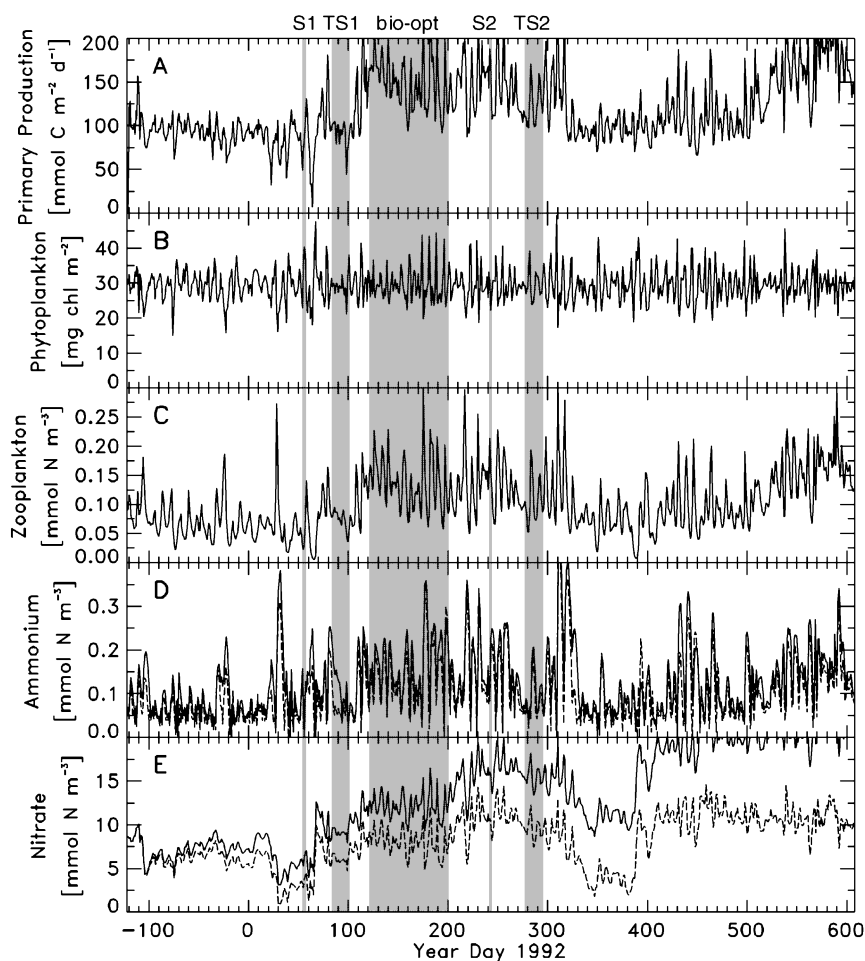
Fig. 8. Simulated time evolution (September 1, 1991) of (A) integrated rate of primary production, (B) integrated phytoplankton chlorophyll, (C) average zooplankton biomass, (D) average ammonium concentration, and (E) average nitrate concentration obtained for the reference simulation. Dashed lines in (D) and (E) represent results assuming a constant horizontal component of ammonium advection of $0.015 \, mmol \, N \, m^{-3} \, d^{-1}$. Shaded regions denote times of the JGOFS EqPac cruises and the fully operational bio-optical mooring.

4.2.3. Model-data comparison

It is difficult to validate marine ecosystem models, since available data on the potentially large number of model components are frequently scarce. However, the suite of biogeochemical measurements available from the JGOFS EqPac experiment (Murray et al., 1994, 1995) provides measurements of most of the dependent variables included in the ecosystem model. These measurements are sufficient to allow comparisons with the simulated distributions on a cruise-averaged basis, as well as comparisons for specific days.

Model-derived values of integrated phytoplankton chlorophyll, average zooplankton biomass, nitrate concentration, ammonium concentration, and integrated primary production, fall within

Table 5
Model-derived values of integrated primary production, integrated phytoplankton, average zooplankton biomass, average ammonium concentration, and average nitrate concentration calculated for the TS1 and TS2 time periods, along with corresponding observations obtained directly from TS1 and TS2 cruise data. Error bars on primary production and phytoplankton data represent standard errors computed by Barber et al. (1996). A $C:N$ ratio of 3 has been applied to the zooplankton data. Ammonim and nitrate concentrations in parentheses were obtained assuming a constant horizontal advection of ammonium of $0.015\,\mathrm{mmol\,N\,m^{-3}\,d^{-1}}$

	Model (TS1)	Data (TS1)	Model (TS2)	Data (TS2)
Integrated primary production ($\mathrm{mmol\,C\,m^{-2}\,d^{-1}}$)	91	90 ± 3	123	129 ± 6
Integrated phytoplankton ($\mathrm{mg\,chl\,m^{-2}}$)	29	29 ± 1	29	33 ± 2
Average zooplanktonbiomass ($\mathrm{mmol\,N\,m^{-3}}$)	0.07	0.07	0.10	0.10
Average ammonium concentration ($\mathrm{mmol\,N\,m^{-3}}$)	0.12(0.06)	0.11	0.10(0.08)	0.07
Average nitrate concentration ($\mathrm{mmol\,N\,m^{-3}}$)	9(6)	6	15(9)	8

ranges for corresponding values calculated for the same time period from the EqPac time series cruise data (Table 5). The model successfully reproduces the 45% increase in both the rate of primary production and in zooplankton biomass, as observed between TS1 and TS2. No change in phytoplankton chlorophyll between the two cruises is predicted by the model; however, Barber et al. (1996) report a small increase in chlorophyll concentration between TS1 and TS2. Both data and simulation results indicate a decrease in ammonium concentration; however, this trend in the model simulation is reversed if a non-zero horizontal ammonium advection is assumed. Nitrate observed during TS2 is $2\,\mathrm{mmol\,N\,m^{-3}}$ greater than that observed during TS1. The reference simulation appears to overestimate nitrate by 3–$7\,\mathrm{mmol\,N\,m^{-3}}$, unless a significant horizontal component of ammonium advection is assumed.

Model-derived values of phytoplankton growth rate, grazing rate, f-ratio, and nitrate uptake, also compare well with corresponding values calculated from JGOFS cruises (Table 6). Model results indicate that phytoplankton growth and grazing rates are depressed by 30–45% early in 1992 when TIWs were not present and El Niño conditions prevailed. The model-derived f-ratios for both spring and fall 1992 are relatively low (0.06–0.15), in agreement with the analysis of McCarthy et al. (1996) which yielded f-ratios in the range 0.06–0.13 during S1, and 0.08–0.20 during S2. Simulated estimates of nitrate uptake integrated to the 1% light level (assumed to be 80 m) were greater in fall 1992 than spring 1992 by 50–75%, also in agreement with the observations. McCarthy et al. (1996) observed this increase in new production between S1 and S2 to be 15 times greater than the corresponding increase in the f-ratio; however, in the simulation the spring/fall increase in new production exceeds that of the f-ratio only by a factor of 3 (1.5) for the survey (time series) cruises. Despite the large differences in new production between the spring and fall cruises, data indicate that nitrate uptake surpassed ammonium uptake by a factor of 8 for both S1 and S2 cruises. Model simulations support these observations. During S1 and S2 simulated nitrate uptake was greater than ammonium uptake by factors of 9 and 7, respectively.

Model-derived values and observations are also consistent on shorter, daily time scales. For instance, because of the relatively high growth and grazing rates (Table 6) of the phytoplankton and zooplankton, the ecosystem model quickly (within a day or two) responds to environmental

Table 6

Model-derived values of phytoplankton growth rate (μ (d^{-1})), grazing rate (K_z (d^{-1})), f-ratio (f), and new production (NP ($mmol\,C\,m^3\,d^{-1}$)) computed for the time periods of the four EqPac cruises, and corresponding values directly calculated from EqPac cruise data. Values are depth-averaged unless a depth is specified, and n.d. indicates no data

	Spring 1992				Fall 1992			
	S1 model	S1 data	TS1 model	TS1 data	S2 model	S2 data	TS2 model	TS2 data
μ	0.4	0.83 (15 m)[a]		0.57 (15 m)[b]		0.98 (15 m)[a]		1.00 (15 m)[b]
		0.34 (45 m)	0.5	0.19 (60 m)	0.9	1.00 (45 m)	0.7	0.85 (30 m)
		0.22 (75 m)				0.32 (75 m)		0.64 (60 m)
K_z	0.2	0.72 (15 m)[a]		0.87 (15 m)[b]		0.57 (15 m)[a]		0.70 (15 m)[b]
		0.22 (45 m)	0.4	0.26 (60 m)	0.6	0.42 (45 m)	0.5	0.57 (30 m)
		0.21 (75 m)				0.27 (75 m)		0.67 (60 m)
f	0.10	0.06–0.13[c]	0.06	n.d.	0.13	0.08–0.20[c]	0.15	n.d.
NP	8	5[c]	6	n.d.	16	19[c]	19	n.d.

[a] From Landry et al. (1995).
[b] From Verity et al. (1996).
[c] From McCarthy et al. (1996).

changes. This is consistent with recent observations from the equatorial Pacific. For instance, data from the IronEx II experiment show chlorophyll concentration doubling within 24 h of the first iron enrichment (Coale et al., 1996b). Supporting data (Behrenfeld et al., 1996) also demonstrate that within these first 24 h the photochemical quantum efficiencies of phytoplankton exponentially increase, with the increase occurring within the extant pico-phytoplankton assemblage.

Agreement also exists between model-derived values of phytoplankton, zooplankton, nitrate, ammonium and primary production and the corresponding daily measurements obtained during the TS1 and TS2 cruises (Fig. 9). During both TS1 and TS2 the magnitude of the variability in the simulated results is similar to that recorded in the data, with the magnitude of this variability being greater during TS2. However, although maximum values for phytoplankton chlorophyll and zooplankton biomass are observed on YD286, these peaks occur 3–4 d earlier (Figs. 9B and C). Thus phytoplankton is first overestimated (YD282) and then underestimated (YD284, YD286). Because of tight P–Z coupling, it is not surprising that a similar trend with a 2-d lag is seen in the zooplankton (Fig. 9C), with first an overestimation (YD284) and then an underestimation (YD286, YD288). The peak in simulated ammonium on YD285 is a result of the underestimation of ammonium uptake by phytoplankton and the overestimation of zooplankton ammonium excretion.

The relationship between primary production and phytoplankton chlorophyll (Fig. 10) provides insight into the coupling between these quantities, and explanations for mismatches between the model results and measurements. The data and simulated values indicate that the two time-series cruises occupy distinct domains when plotted in terms of primary production versus phytoplankton chlorophyll. Specifically, TS1 has lower absolute *and* specific rates of primary productivity. Our modeling results support the hypothesis of Barber et al. (1996), which states that the lower rates of primary production measured during TS1 are due to lower iron concentrations resulting
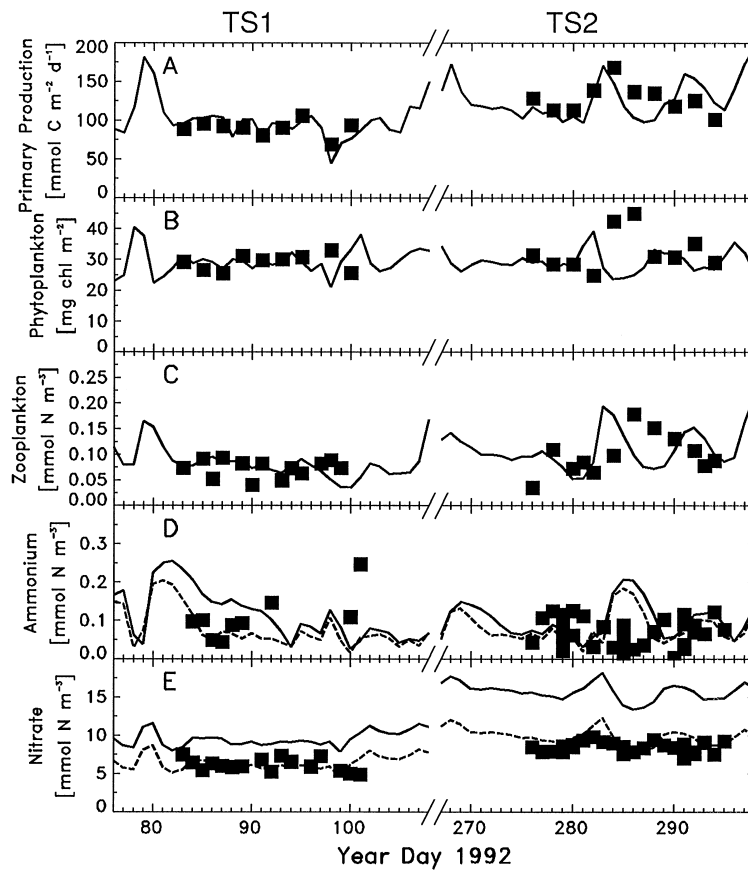
Fig. 9. Simulated time distributions of (A) primary production, (B) phytoplankton chlorophyll, (C) zooplankton, (D) ammonium, and (E) nitrate, corresponding to the TS1 and TS2 cruise times. The corresponding measurements from the two cruises (■) are shown. Dashed lines in (D) and (E) represent results assuming a constant horizontal component of ammonium advection of 0.015 mmol N m^{-3} d^{-1}.

from the deeper thermocline associated with the presence of El Niño conditions during this time period.

The greater variability in phytoplankton chlorophyll observed during the second time-series cruise is also predicted by the model, with the highest (39.3 mg chl m^{-2}) and lowest (23.8 mg chl m^{-2}) chlorophyll values at 0°N, 140°W occurring during TS2 (Fig. 10A). However, the simulations do not reproduce the slightly higher average chlorophyll concentrations observed during TS2 as compared to TS1 (Fig. 10B). A possible explanation for both the increased phytoplankton variability during TS2 as well as the model–data mismatch of average chlorophyll concentration, lies in the passage of a TIW across 0°N, 140°W during TS2 (Figs. 2 and 7D), and its possible effect on the phytoplankton community. Meridional velocity, a primary indicator of instability wave activity, and chlorophyll concentration are highly correlated both during TS2 as well as during the deployment of the bio-optical mooring (Fig. 11). Excluding observed and simulated primary production and chlorophyll values for those days during which the TIW passed
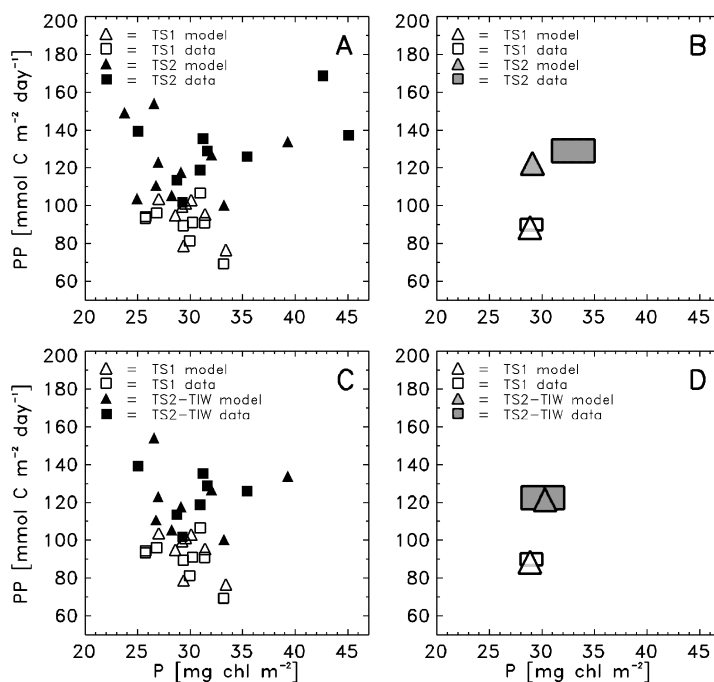
Fig. 10. Model-data comparison of phytoplankton chlorophyll (P) versus primary production (PP) at $0°$N, $140°$W. Data are from Barber et al. (1996). (A) Daily comparison for TS1 and TS2 cruise time periods. (B) Comparison of cruise-averaged values for TS1 and TS2 time periods; shaded rectangles represent average of data, where the size of symbol indicates the magnitude of the standard error (Barber et al., 1996). (C) As in (A), except TS2 data and model results are shown excluding days between YD282 and YD288, which is the time period during which the TIW passed by $0°$N, $140°$W. (D) As in (B), except TS2 data and model averages are computed excluding days between YD282 and YD288.

across $0°$N, $140°$W (YD282–YD288), substantially improves the model–data comparison (Figs. 10C and D). The exclusion of these data in the computation of the cruise averages (Fig. 10D), also serves to illustrate the isolated effect of El Niño conditions on the equatorial ecosystem: absolute *and* specific rates of primary productivity decrease, but phytoplankton chlorophyll remains at a constant background level. The higher phytoplankton chlorophyll concentration observed during TS2 (Fig. 10B) is due to a higher frequency mesoscale event: the passage of the instability wave.

In the following section, three idealized modeling experiments are presented which are designed to provide insight into the effects of variations in iron concentration, species composition, and vertical velocity, on the rate of primary production, chlorophyll concentration, and zooplankton biomass in the central equatorial Pacific.

4.3. Idealized modeling experiments

4.3.1. Iron concentration

To examine the effect of different levels of iron concentration on an ecosystem in the central equatorial Pacific, the iron input time series was varied such that concentration at the base
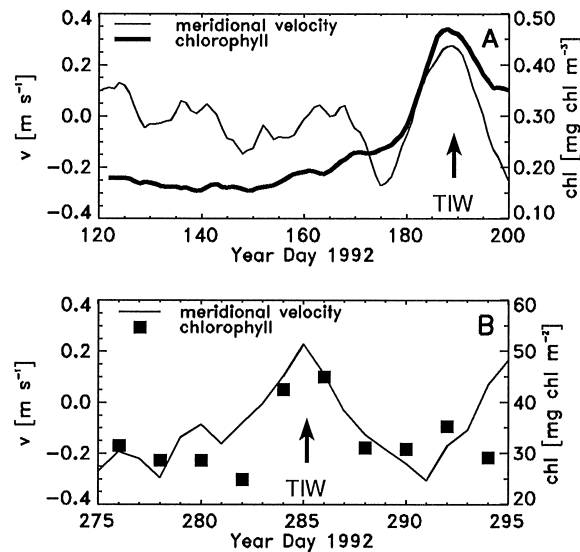
Fig. 11. (A) Low-pass filtered TAO meridional velocity and chlorophyll concentrations computed using the 45 m fluorometric measurements collected from the bio-optical mooring (Foley et al., 1997) and (B) TAO meridional velocity at 25 m depth and integrated chlorophyll concentration (Barber et al., 1996) during the TS2 cruise. During the TIWs, both time series show a positive correlation between strong northward velocities and increased chlorophyll concentration.

of the euphotic zone was reduced from 100 to 25 nmol Fe m^{-3} over 30 d, remained at this concentration for 3 months, and then increased over 30 d to 100 nmol Fe m^{-3} (Fig. 12A). This gradual change in iron concentration produces significant changes in the model ecosystem, the most notable of which is a 20% drop in the level of primary production (Fig. 12B). More interestingly, the decrease in iron does *not* effect a decrease in phytoplankton chlorophyll (Fig. 12C), but does cause a significant (26%) drop in zooplankton biomass (Fig. 12D). This results from the similarly high growth rates and response times of both the picoplankton and microzooplankton. Because grazing pressure tends to drop off nearly as quickly as primary production, simulated phytoplankton chlorophyll remains at a constant background level, despite lower iron concentrations.

The ecosystem model would respond similarly to a 75 nmol Fe m^{-3} increase in iron concentration, e.g. on monthly time scales phytoplankton concentration would remain at a constant background level, whereas primary production and zooplankton biomass would increase substantially. However, such elevated iron concentrations (O(175 nmol Fe m^{-3})) lasting over these time scales (O(3 months)) would be unlikely to occur naturally in the central equatorial Pacific, where such iron concentrations generally only occur well beneath the bottom of the euphotic zone, i.e. below 150 m (Gordon et al., 1997). Although data from the IronEx II iron enrichment experiment indicate that in the short term (O(days)) a large increase in iron concentration may result in large increases in phytoplankton chlorophyll, these data cannot be used to assess the effect of high iron concentrations on phytoplankton chlorophyll on monthly/annual time scales (Fig. 12).
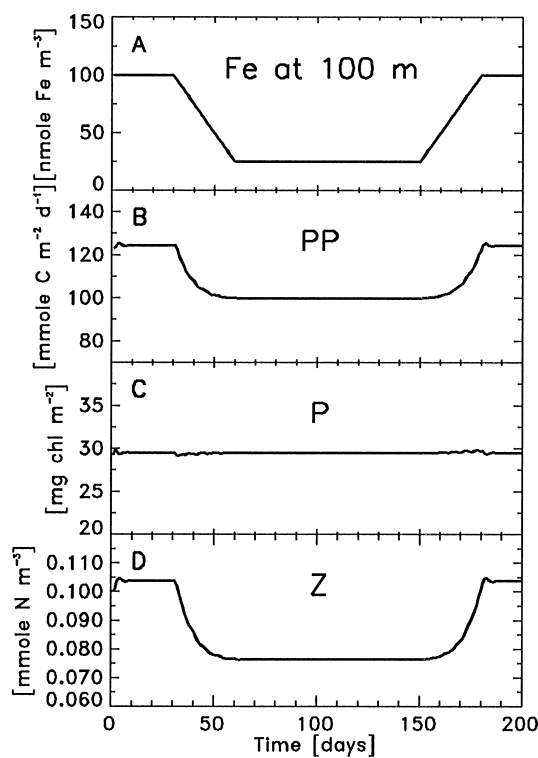
Fig. 12. Time-varying distributions of (A) idealized iron (*Fe*) input used to force ecosystem model, and the resultant (B) simulated primary production (PP), (C) simulated phytoplankton chlorophyll (*P*), and (D) simulated zooplankton concentration (*Z*).

4.3.2. Species composition

An assumption of the ecosystem model used in this analysis is that the species compositions of the phytoplankton and zooplankton populations remain fixed. Thus, because it is not possible to directly simulate a change in species composition with this simplified model, it is not possible to investigate why species compositions change. However, it is possible to examine the ramifications of such a change by varying certain parameter values, and thus indirectly simulating the effects of a change in species composition.

The model, as configured, represents a phytoplankton community that consists of picoplankton and microzooplankton, but under certain environmental conditions diatoms and mesozooplankton have been observed to become abundant in the equatorial Pacific (Iriarte and Fryxell, 1995; Bidigare and Ondrusek, 1996). This change in community structure can be reproduced by increasing the half-saturation coefficient of iron uptake from 34 to 47 nmol Fe m^{-3} over two weeks (starting on YD281), a value which is consistent with a 15% diatom population (Price et al., 1991; Fitzwater et al., 1996; Coale et al., 1996), and then decreasing the value to 34 nmol Fe m^{-3}. Since diatoms are less vulnerable to microzooplankton grazing, and mesozooplankton have a longer response time, the grazing rate is also temporarily lowered over this same time period. These changes in parameter values are applied to an otherwise steady-state model run (Fig. 13A), i.e.
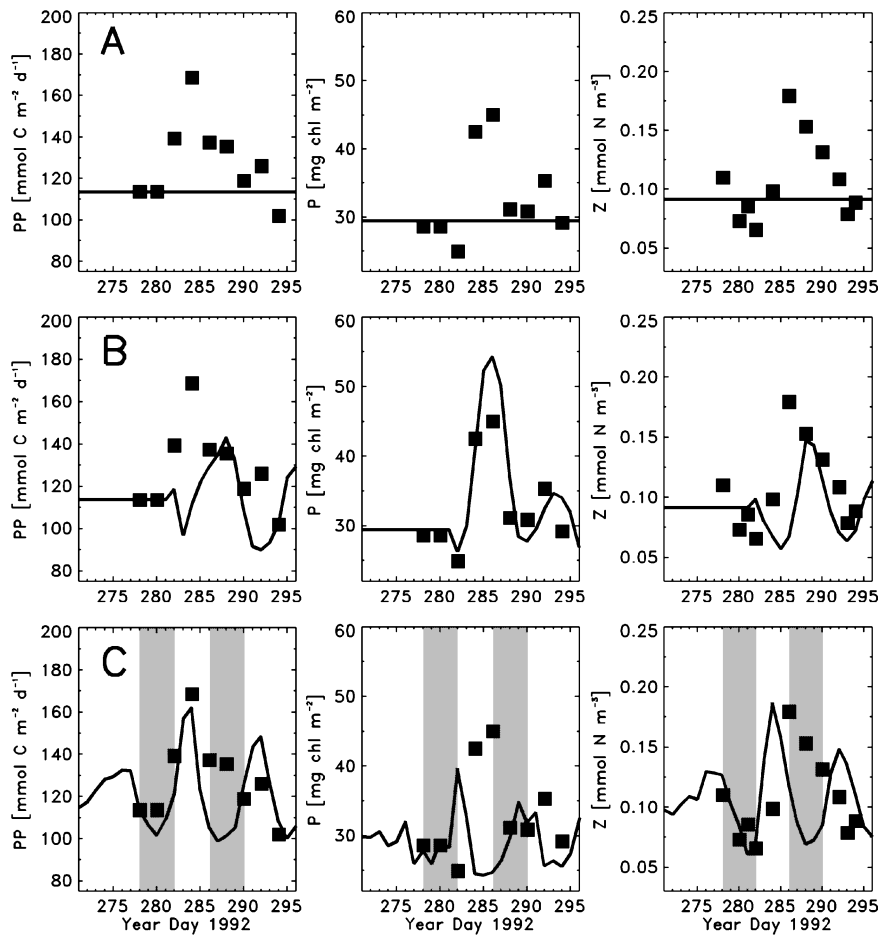
Fig. 13. Simulated time series of primary production (*PP*), phytoplankton (*P*), and zooplankton (*Z*). (A) Simulations using constant forcing, (B) as in (A) except iron uptake kinetics (k_{Fe}) and zooplankton grazing (g) are varied, and (C) as in (A) except high–pass filtered vertical velocities and iron concentrations are used as forcing functions. Periods of upwelling are denoted by shaded regions and observations from the EqPac TS2 cruise are indicated by ■.

constant upwelled iron, vertical velocity, nitrate advection, and light. In order to examine the ramifications of such a rapid (O(days)) change in species composition, simulation results over the time period YD270–YD295 are shown in Fig. 13.

Relative to the simulation in which parameter values are not varied (Fig. 13A), the increase in percent diatom abundance, simulated by changing parameter values, has a large effect on the rate of primary production, total phytoplankton chlorophyll, and zooplankton biomass (Fig. 13B). Because iron concentration remains fixed, initially primary production drops by 20% between YD281 and YD283 as a result of the increased need for iron in order to support diatom growth. This evokes a corresponding decrease in chlorophyll. Lower grazing rates, however, tend to decrease zooplankton biomass effecting a near doubling of total chlorophyll concentration between YD282 and YD286, as well as a substantial increase in primary production. As mesozooplankton eventually respond to the increase in diatom abundance, grazing rate and total

zooplankton biomass increase causing a decrease in chlorophyll and eventually primary production. The decrease in phytoplankton biomass (diatoms) causes a further drop in primary production which reaches a minimum on YD292.

4.3.3. Vertical velocity

The effects of high-frequency variations in vertical velocity are examined by forcing the model with the high-pass filtered vertical velocity and iron time series (Figs. 7G–I). The resulting simulated time series (Fig. 13C) show that during both upwelling events (YD278–YD282 and YD286–YD290) average zooplankton biomass decreases by nearly 50%. This is because of the linear decrease in zooplankton concentration with depth (Fig. 6C); during periods of upwelling, water with relatively low concentrations of zooplankton upwells at the base of the euphotic zone, replacing shallower water that contains higher concentrations of zooplankton biomass. At the same time, much-needed micronutrients, e.g. iron, are upwelled, thereby stimulating primary production and increasing both phytoplankton and, eventually, zooplankton biomass. When downwelling conditions prevail (YD283–YD286) the opposite scenario occurs. The simulated average zooplankton biomass initially increases due to the downwelling of high-concentration surface waters. Simultaneously, however, the supply of micronutrients is shut off, resulting in a decrease in simulated primary production, phytoplankton chlorophyll, and eventually zooplankton biomass.

The results of these simulations thus suggest that high-frequency oscillations in vertical velocity and iron concentration may cause similar high-frequency oscillations in the rates of primary production, phytoplankton chlorophyll and zooplankton biomass. Further evidence of this is shown in the chlorophyll concentrations obtained from the bio-optical mooring at 0°N, 140°W. These data (Fig. 14) exhibit a strong 7-d periodicity which is seen in the simulated plankton time series (Fig. 13C), and are associated with corresponding high-frequency oscillations in the time series of derived-iron concentration (Fig. 7I).

5. Discussion

An advantage of using a relatively simple biological–physical model is that the specific mechanisms underlying observed patterns in simulated distributions are easily identifiable. Using the results of the idealized modeling experiments described above, the effects of various environmental forcing mechanisms can be isolated and quantified. Specifically, the discussion will include the effects on plankton concentrations and primary production of (a) interannual variability in the depth of the thermocline, (b) upwelling variability and horizontal advection associated with tropical instability waves, and (c) high-frequency vertical velocity variability due to equatorially trapped internal gravity waves. Finally, after examining each of these time scales individually, the superposition of these processes will be discussed.

5.1. Interannual variability: El Niño

Determination of the effect of an El Niño on a marine ecosystem is problematic. These events have interannual periodicities, yet phytoplankton and zooplankton have doubling rates on the
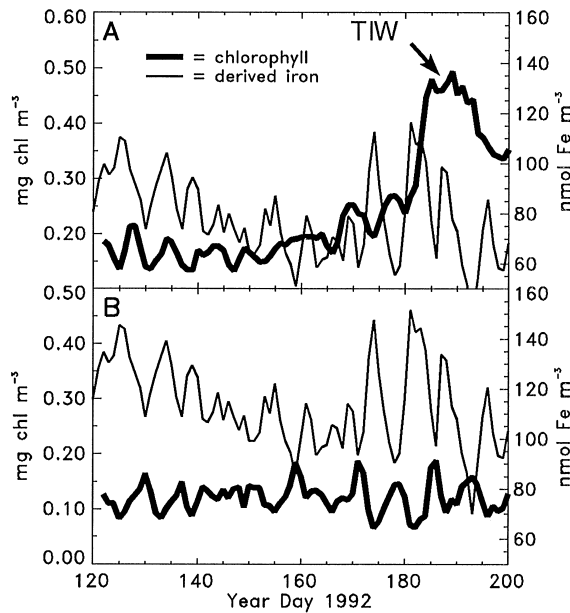
Fig. 14. Time series of chlorophyll concentration obtained from fluorometers on the bio-optical mooring at 140°W (Foley et al., 1997), and iron concentration computed from $T:Fe$ relationship at (A) 45 m and (B) 80 m.

order of days which causes most traditional biological observations to be taken on time scales of hours to days. Because of this mismatch in time scales, it is difficult to isolate the effects of an El Niño on the equatorial Pacific ecosystem at 140°W solely from a series of four cruises, such as occurred during EqPac; however, a biological–physical model which resolves processes on daily/weekly time scales can provide insight into this difficult problem.

Although a typical El Niño evokes multiple changes in the physical environment of the equatorial Pacific, the most crucial change for biological processes is the deepening of the thermocline; a deeper thermocline translates directly into a decrease in iron supply, since iron is primarily upwelled from the Equatorial Undercurrent (Barber et al., 1996). The ramifications of this single phenomenon are evident in the simulated response of the model ecosystem to a slow (O(months)) change in iron concentration (cf. Fig. 12), as might result from a gradual deepening of the thermocline during an El Niño. For instance, the deeper thermocline and lower iron concentrations cause primary production to drop by nearly 20% (Fig. 12). The reference simulation (Fig. 9; Table 5) shows that on average, the rate of primary production is 25% lower during TS1 than TS2 and also indicates that this is a direct result of a deeper thermocline and correspondingly lower iron concentrations during TS1 (45 nmol Fe m^{-3} at 100 m) than during TS2 (97 nmol Fe m^{-3}).

These results support Barber et al. (1996) who hypothesized that a deepening of the thermocline, as might be associated with an El Niño, could be responsible for a substantial drop in primary productivity. This decrease in primary production is seen in the simulated distributions that assume a constant species composition. This suggests that the species composition of the phytoplankton assemblage is not likely to be a primary factor regulating variations in primary production during El Niño versus non-El Niño conditions.

A decrease in phytoplankton biomass could result from a drop in the rate of primary production; however, no such decrease is observed in the idealized modeling experiment results shown in Fig. 12. Because of the tight coupling between phytoplankton and zooplankton and the high growth rates of both, grazing pressure and zooplankton biomass tend to drop nearly as rapidly as primary production. When combined with lower phytoplankton production, this drop in grazing pressure causes simulated phytoplankton chlorophyll to remain at a constant background level, despite the lower iron concentrations (Fig. 12). Thus the El Niño (deep thermocline) and non-El Niño (shallow thermocline) time periods can be thought of as two different realizations of the background state of the ecosystem. In both of these cases micro-grazers control the picoplankton, resulting in a constant background level of phytoplankton chlorophyll; however, the rate of primary production is determined by the iron concentration in the euphotic zone, which in turn is governed by the depth of the thermocline.

The significant difference in chlorophyll concentrations observed on TS1 versus TS2 (Fig. 10B), thus cannot be explained via the presence of El Niño conditions during TS1. Instead, the simulations (Figs. 10C and D) suggest that this perturbation of the background state may result from higher frequency processes, as discussed in the following section.

5.2. Tropical instability waves

Throughout the second half of 1992, the variability in the meridional velocity time series at 10 m (Fig. 2) and 25 m (Fig. 7A) is dominated by TIWs. Sensors located on the bio-optical mooring provide time series that illustrate the association of northward velocities with higher phytoplankton chlorophyll during the passage of one such TIW (Fig. 11A). The TS2 cruise was carried out during the passage of a relatively weak TIW, but increased chlorophyll levels are still associated with northward velocities (Fig. 11B). Similarly, during S2 the highest integrated water column chlorophyll values were located at 1°N (45 mg chl m^{-2}; Bidigare and Ondrusek, 1996) and were likewise associated with the highest northward velocities (>20 cm s^{-1}) recorded along the 12°N–12°S acoustic Doppler current profiler transect (Johnson, 1996).

Data from the EqPac cruises also suggest that these increased chlorophyll levels that are associated with the TIWs (Fig. 11) may be related to changes in species composition. Between YD280 and YD286, chlorophyll concentration increased by 60%, while fucoxanthin, a known marker for diatoms, increased by 170% (Bidigare and Ondrusek, 1996). Diatom cell abundance at the surface was generally less than 1500 cells l^{-1} during the TS1 and TS2 cruises. However, by YD287 this abundance had nearly quadrupled to 7500 cells l^{-1} before eventually returning (YD295) to levels similar to those recorded earlier in the TS2 cruise (YD278) and throughout the TS1 cruise (Iriarte and Fryxell, 1995). Likewise, during S2 the strongest northward velocities (1°N; Johnson, 1996) were associated with a 300% increase in chlorophyll contribution by diatoms (Iriarte and Fryxell, 1995).

Since the ecosystem model used in this analysis assumes a priori that the phytoplankton and zooplankton species compositions are constant, the model cannot be used to investigate the reasons why increases in diatom abundance were observed. However, by varying certain parameter values (i.e. k_{Fe} and g), it is possible to indirectly simulate the potential effects of a change in species composition, such as that observed during TS2. These simulation results (Fig. 13B) suggest that an increase in percent diatoms can lead to a substantial increase in chlorophyll concentration, similar

to that observed during TS2. Although an increase in diatom cell abundance results in a substantial increase in total phytoplankton chlorophyll, the specific mechanisms underlying this change in species composition are not known and cannot be assessed solely by the five-component ecosystem model used in this analysis. However, possible explanations for the mechanisms underlying this change in species composition can be suggested based on the available EqPac data sets and the time series of iron concentration and vertical velocity derived in this analysis.

Because diatoms have larger requirements for iron uptake (Morel et al., 1991; Fitzwater et al., 1995; Coale et al., 1996a) and are less susceptible to grazing by the dominant microzooplankton than are the smaller picoplankton (Landry et al., 1995; Verity et al., 1996; Coale et al., 1996b), a substantial increase in iron concentration would be expected to lead to enhanced in situ growth of diatoms and a resulting increase in diatom biomass (Cullen et al., 1992). In fact, such a change in species composition was observed during the open ocean iron enrichment experiments carried out in 1993 (IronEx I) and 1995 (IronEx II), during which 450 kg of iron (as acidic iron sulfate) was added to equatorial Pacific waters near 90–110°W (Martin et al., 1994; Coale et al., 1996b). Therefore, if an increase in iron concentration was associated with the passage of the TIW, this might explain the increase in diatom biomass observed during TS2.

In the central equatorial Pacific, the source of iron is believed to be located at depth (Barber et al., 1996). Therefore, if the increase in diatom abundance was solely due to in situ growth, the peak in diatom abundance would be expected to be associated with a peak in upwelling velocity. Unfortunately, there are no direct measurements available in this region to either support or refute this hypothesis. However, the vertical velocities indirectly derived in this analysis indicate that the large peak in diatom abundance observed during TS2 (YD282–YD289) does *not* correspond temporally to a peak in upwelling velocity (Fig. 7D). Instead, this time period of greatest diatom abundance, increased chlorophyll concentration, and strong northward velocity (Fig. 11) corresponds to *downwelling* in the upper water column (Fig. 7D). This suggests that the increase in diatom abundance associated with TIWs is not due solely to in situ growth. On the contrary, the spatial/temporal separation between upwelling and increased diatom abundance indicates that a combination of mechanisms, e.g. in situ growth and advection, must be invoked to explain the observed changes in speciation.

The correlation of strong northward velocities with high rates of downwelling is not limited to the time period of the TS2 cruise (Figs. 7A and B). Rather, this correlation is a general characteristic of strong TIW activity (Weisberg and Qiao, 2000), and can be explained as follows. Tropical instability waves are typically associated with strong advective fronts, which are located along the leading edges of the waves and are oriented from northeast to southwest (Legeckis, 1977; Yoder et al., 1994; Flament et al., 1996). Southeast of these fronts, relatively cold and nutrient-rich equatorial water moves northward, while northwest of the fronts relatively warm and nutrient-poor equatorial countercurrent water moves southward (Johnson et al., 1996; Archer et al., 1997). As a result of this circulation pattern, strong convergences are centered at the fronts, where cold nutrient-rich water moves northward and sinks below warmer water to the north (Archer et al., 1997). On the trailing (eastern) sides of the wave cusps, meridional divergences lead to zones of strong upwelling. Thus, as TIWs advect past 0°N, 140°W from east to west, time-series measurements at this location reveal oscillations between northward/downwelling velocities and southward/upwelling velocities (Figs. 7A and B).

Although direct measurements of iron are not available, it is likely that the localized upwelling zones associated with the TIWs contain unusually high concentrations of iron, thus stimulating the growth not only of the dominant picoplankton, but eventually of the diatoms as well. Because the upwelling zones are regions of divergence, this high-nutrient water may advect northward toward the convergent front located on the leading (western) edge of the TIW. Meanwhile, because microzooplankton are unable to graze the diatom population, and because some species of diatoms (e.g. *Rhizosolenia* sp.) are buoyant, diatom abundance may continue to increase, reaching a maximum near the convergent (downwelling) front. Thus, time-series measurements at 0°N, 140°W would be expected to indicate a tight correlation not only between northward and downwelling velocities, but also between northward velocities and high chlorophyll concentrations (Fig. 7A and B), and specifically high diatom abundance.

This scenario is supported by the results of a number of other EqPac studies. For instance, EqPac TS2 data do indicate a strong correlation between increased diatom abundance and strong northward velocities. The increase in chlorophyll contribution by diatoms from $1.3 \, \text{mg chl m}^{-2}$ (YD278) to $4.3 \, \text{mg chl m}^{-2}$ (YD287) (assuming a ratio of $70 \, \text{mg C} : \text{mg chl}$) (Iriarte and Fryxell, 1995) is associated with a change in meridional velocity from $-20 \, \text{cm s}^{-1}$ (YD278) to $+20 \, \text{cm s}^{-1}$ (YD287) (Fig. 2). It is also interesting to note that this temporal variation in diatom chlorophyll observed during TS2 is very similar to the spatial variation in diatom chlorophyll observed during the S2 cruise which crossed the convergent TIW front near 2°N, 140°W. Data from S2 indicate that the chlorophyll contribution by diatoms increases from less than $1 \, \text{mg chl m}^{-2}$ at 1°S (south of the SW–NE oriented front) to nearly $6 \, \text{mg chl m}^{-2}$ at 2°N (Bidigare and Ondrusek, 1996).

As the instability wave passed 140°W during TS2, Iriarte and Fryxell (1995) also observed the maximum cell numbers of diatoms shifting downward from 15 m on YD283, to 45 m on YD289, and 60 m depth on YD295. They also suggest that the observed enrichment of cell numbers of diatoms in the upper 45 m layer probably resulted from a lateral water mass displacement due to the passage of the TIW, rather than in situ enhancement of growth rates. Furthermore, a simple gas (O_2, CO_2) exchange model constrains the maximum atmospheric exposure time of these waters to 10–20 d (Archer et al., 1997). Measurements of ^{234}Th within the waters of the front (Archer et al., 1997) also suggest that a water parcel within the front had only a short residence time (less than 3 d) before subduction, and that much of the standing stock of particulates must have been imported as particles, rather than growing in place.

In summary, the simulation results and observations presented above are consistent with the idea that a zone of localized divergence and upwelling associated with the TIW increases iron concentration in the euphotic zone. As this iron-enriched water travels toward the convergent front, growth of both the picoplankton and eventually the diatoms is stimulated, increasing total chlorophyll concentration. Diatom biomass continues to increase as this water advects northward toward the convergent front, and begins to downwell beneath the northern low-nutrient water. In this scenario, the water with the highest diatom biomass is associated with northward downwelling velocities and both in situ growth and horizontal advection play crucial roles in explaining the existence of the spatial and temporal gradients in chlorophyll concentration associated with TIWs.

Unfortunately, it is not possible to determine the net effect of TIWs on export production, using the single-species model developed in this analysis. However, Archer et al. (1997) have found that very high rates of export production are associated with the cold waters located on the south side of the convergent TIW front. Similarly, using data from both the EqPac and Zonal Flux studies, as

well as from the French JGOFS FLUPAC equatorial Pacific cruise in October 1994, Dunne et al. (2000) find that new production and particle export are both twice as high during periods of strong TIW activity. In fact, variability in particulate organic carbon export appears to be more highly correlated to TIW activity than to large-scale variability associated with El Niño conditions.

5.3. Equatorially trapped internal gravity waves

The reference simulation shows considerable variability at frequencies even higher than that of the TIWs. This variability is a direct response to the high-frequency variability of the vertical velocity and iron input time series (Figs. 7G–I). Such oscillations are consistent with the period (6–8 days) and latitudinal structure of equatorially trapped internal gravity waves (IGWs) of the first baroclinic vertical mode (Wunsch and Gill, 1976).

Since these waves are often of little interest to oceanographers studying conservative properties such as density and temperature, this high-frequency variability is often considered to be merely noise and is typically removed from time series (e.g. McPhaden, 1993; Kessler and McPhaden, 1995; Foley et al., 1997; Weisberg and Qiao, 2000). However, because the doubling time of the dominant picoplankton in the equatorial Pacific is short (1–2 d), these high-frequency waves can potentially explain much of the variability observed in both phytoplankton chlorophyll levels and primary production, and are therefore worthy of further exploration.

The effect of these vertically oscillating waves on phytoplankton is two-fold: (1) as iron-enriched water is advected higher into the euphotic zone where there is ample light for photosynthesis, phytoplankton growth will be stimulated, and (2) because phytoplankton biomass decreases sharply below 70 m (Fig. 6) the vertical advection of phytoplankton biomass will cause chlorophyll levels below 70 m to increase during periods of downwelling, and decrease during upwelling due to dilution with deeper low-chlorophyll waters. The former process, in situ growth, might dominate in regions of low iron concentration and/or low vertical chlorophyll gradients, such as at the depth of the deep chlorophyll maximum (40–50 m). Deeper in the euphotic zone (80–100 m), where iron concentrations and vertical gradients of chlorophyll are relatively high, the dilution effect would be expected to dominate.

Subsurface time series from the bio-optical mooring provide information which may be used to directly assess the impact of these waves on the phytoplankton community. At 80 m, temperature and chlorophyll concentration, as derived from fluorometric measurements (Foley et al., 1997), are highly correlated (correlation coefficient of 0.7) and in phase. Because of the $T : Fe$ relationship used in this analysis, it is not surprising to see that derived-iron and chlorophyll concentration are inversely correlated, i.e. higher iron concentrations are associated with lower chlorophyll concentrations with a correlation coefficient of 0.7 (Fig. 14B). These observations support the idea that the dilution effect dominates at 80 m, near the base of the euphotic zone.

Time series obtained from sensors located at 45 m on the bio-optical mooring, reveal that chlorophyll concentration and temperature at this depth are inversely correlated with a 2-d time lag. (The maximum chlorophyll concentration occurs 2 d after the minimum temperature recorded; the correlation coefficient is -0.7.) Thus it is not surprising to see that at this depth, derived iron and chlorophyll are positively correlated, with chlorophyll lagging iron concentration by roughly two days (Fig. 14A). During the latter portion of these time series (YD180–YD200) a TIW dominates the chlorophyll signal; however, during the early portion of these records iron and

chlorophyll are positively correlated (correlation coefficient is 0.6 from YD125–YD145, and 0.4 from YD125–YD155) with chlorophyll lagging iron by 2 d. These data thus support the idea that in situ growth may be the dominant mechanism explaining the observed variability in chlorophyll concentration at 45 m depth.

Although IGWs persist throughout the two-year model run, their effect on iron concentration is reduced when El Niño conditions produce a deeper thermocline. These waves thus play a larger role in explaining phytoplankton variability during TS2 than during TS1. In fact, two such waves occurred during the TS2 cruise. These events are evident in the high-pass filtered time series of vertical velocity (Figs. 7G–I), yet their signal is removed by standard filtering techniques (Figs. 7A–F).

The isolated effect of these high-frequency waves can be examined by forcing the model with the high-pass filtered time series of vertical velocity and iron concentration (Figs. 7G–I). The results of this simulation (Fig. 13C) indicate that IGWs may cause variations in integrated phytoplankton chlorophyll on the order of $10\,mg\,chl\,m^{-2}$. (Assuming a euphotic zone depth of roughly 100 m, this corresponds to variations in average phytoplankton chlorophyll on the order of $0.1\,mg\,chl\,m^{-3}$). Specifically, during periods of upwelling (YD278–YD282 and YD286–YD290) simulated zooplankton biomass initially decreases due to dilution with deeper, low-zooplankton waters (Fig. 13C); however, primary production and chlorophyll increase, as upwelling provides micronutrients necessary for phytoplankton growth. Eventually this increase in phytoplankton also stimulates an increase in zooplankton biomass (YD281–YD282 and YD288–YD290). For downwelling conditions (YD283–YD286), the situation is reversed. Initially, the average concentration of zooplankton biomass increases, as high concentration waters are mixed downwards. Furthermore, the IGW-induced iron supply is shut off, slowing the rate of primary production. Together, these processes effect a 40% decrease in integrated phytoplankton chlorophyll, which ultimately causes a decrease in zooplankton biomass.

Although a change in species composition was required to reproduce the observed TIW-induced variability (20–30 d) in phytoplankton biomass, the high-frequency variability resulting from the IGWs appears to be explained without such species changes. This difference arises because over such short time periods (6–8 d), the relatively low growth rate of the diatoms prohibits them from increasing fast enough to have a significant impact on the population composition. While the pulses of iron caused by IGWs are large enough to stimulate pico- and nanoplankton growth, they are orders of magnitude smaller than those induced by the IronEx fertilization experiments (Martin et al., 1994; Frost, 1996) and those typically used in laboratory experiments (Martin et al., 1989; Greene et al., 1991; Chavez et al., 1991) where diatom blooms have been recorded. Thus, although these waves may increase the background levels of primary production, they do not perturb the community composition as do the TIWs, and therefore they probably have little influence on export production.

Estimating the net effect of IGWs on the plankton community is difficult. Since the heat content of the water near the base of the euphotic zone is approximately a conservative property over time scales of 6–8 d, the net increase in temperature due to downwelling would be expected to approximate the net decrease in temperature due to upwelling over these time scales. Therefore, such waves are rarely significant when studying average heat balances at this depth, and are typically filtered out of heat budget calculations (Kessler and McPhaden, 1995). However, this may not be the case for a non-conservative property such as iron concentration. If iron is taken up

within the upper euphotic zone, then it is possible that less iron will be downwelled than was originally upwelled. Given this asymmetry, IGWs may potentially provide a significant net source of iron, even if net downwelling conditions prevail. This mechanism for increasing iron concentration in the upper euphotic zone of the equatorial Pacific is analogous to the important mesoscale process of eddy pumping (McGillicuddy et al., 1999; Siegel et al., 1999) in which eddies induce isopycnal displacements that lift cold nutrient-rich waters into the euphotic zone, driving new primary production in the North Atlantic.

The model used in this analysis cannot explicitly test this hypothesis since it does not contain a separate iron model; iron itself is never 'used up', but is rather parameterized as a function of instantaneous temperature at depth. Numerical experiments, however, can be carried out which reveal upper and lower bounds on the effects of these waves on phytoplankton biomass and productivity. For instance, given the iron concentrations and vertical velocities computed as part of this analysis, the average iron flux into the euphotic zone for the year of 1992 is 109 nmol $Fe\,m^{-2}\,d^{-1}$. This value is consistent with the range of 86–155 nmol $Fe\,m^{-2}\,d^{-1}$ (Gordon et al., 1997) computed using the constant vertical velocities of Bryden and Brady (1985) shown in Fig. 5. However, if all iron advected into the euphotic zone is assumed to be used, and therefore downwelling no longer represents a significant sink of iron, the average iron flux into the euphotic zone more than doubles: from 109 to 389 nmol $Fe\,m^{-2}\,d^{-1}$. This value is clearly an upper bound on the amount of iron advected into the euphotic zone. More realistically, one might assume that everything above 80 m is used, since this represents the average depth above which iron is typically undetectable (Gordon et al., 1997). In this case, the average iron flux for 1992 is 219 nmol $Fe\,m^{-2}\,d^{-1}$.

The importance of internal gravity waves as a source of iron for the euphotic zone can be estimated if monthly averaged vertical velocities (as might be available from OGCM output) are used to compute these iron fluxes, in place of the daily vertical velocities derived in this analysis. If all iron above 80 m is assumed to be taken up by the phytoplankton, using monthly averaged vertical velocities results in an iron flux into the euphotic zone for the year of 1992 of only 161 nmol $Fe\,m^{-2}\,d^{-1}$. Comparing this with the value obtained if daily vertical velocities are used (219 nmol $Fe\,m^{-2}\,d^{-1}$), suggests that if monthly averaged vertical velocities are used in place of daily velocities, iron flux may be underestimated by 30%. Thus, if these high-frequency waves are not resolved, as is the case when ecosystem models are forced by or coupled to OGCMs, iron fluxes may be seriously underestimated. In such coupled systems the effect of these waves on the biology may need to be parameterized.

5.4. Superposition of processes

In the central equatorial Pacific, plankton concentrations and rates of primary production are simultaneously affected by processes on many different time scales, including interannual El Niño variability, 20–30 d TIWs, and 6–8 d IGWs. Throughout TS1 El Niño conditions prevailed, TIWs were nearly non-existent, and the effects of IGWs were substantially reduced as a result of a relatively deep thermocline. By TS2, El Niño conditions had subsided. During this second cruise both TIWs and IGWs significantly impacted the plankton community. Simulation results (cf. Fig. 12B) indicate that lower iron concentrations associated with the deeper thermocline resulting from the 1991–92 El Niño, are primarily responsible for the lower productivities observed during TS1 as
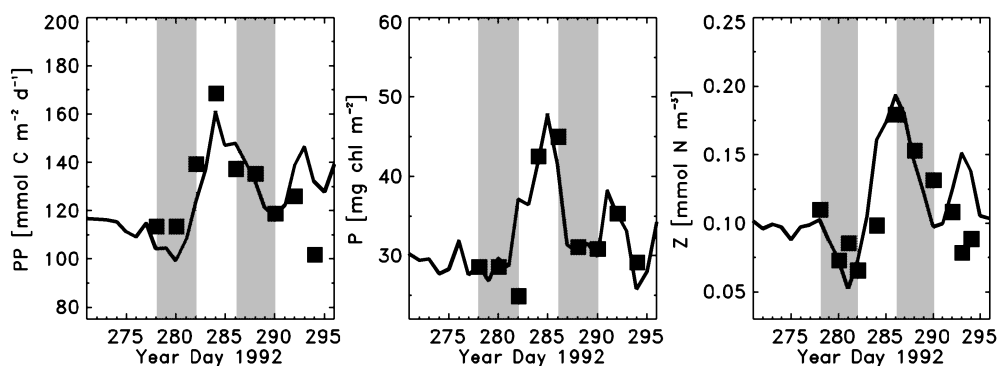
Fig. 15. Simulated time series of primary production (*PP*), phytoplankton (*P*) and zooplankton (*Z*) that include the effects of El Niño and IGWs (via forcing by daily (unfiltered) vertical velocities and iron concentrations), as well as TIWs (via variable iron uptake kinetics and zooplankton grazing as in Fig. 13B). Periods of upwelling are denoted by shaded regions, and observations from the EqPac TS2 cruise are indicated by ■.

compared to TS2. However, the shallower thermocline occurring during TS2 does not appear to be the cause of the higher phytoplankton concentrations observed during this cruise. Chlorophyll levels appear to be more dependent on higher frequency events such as changes in speciation due to TIWs (Fig. 13B) and pulses of iron due to IGWs (Fig. 13C), than on El Niño-related variations in thermocline depth (Fig. 12C). Both primary production and zooplankton biomass are also affected by these relatively high-frequency processes. In fact, only when the effects of all these processes are superimposed, does the model successfully reproduce primary production, phytoplankton and zooplankton data from the TS2 cruise (Fig. 15).

6. Summary and conclusions

The equatorial Pacific Ocean is characterized by physical variability spanning a wide range of time scales, from strong interannual variability (El Niño) to oscillations on weekly time scales (equatorially trapped internal gravity waves). Biological data sets collected in this region are affected by motions on all these time scales simultaneously; the effects of these various processes are superimposed, and there is a transfer of energy between the largest and smallest scales. As a result it is difficult, if not impossible, to determine from discrete samples made at distinct times (e.g. cruises), which type of physical variability is causing what response in the biological community. Numerical models, however, provide a means to isolate individual biological responses to these various forcing mechanisms and to quantify the respective contributions from each of these processes.

In order to examine the effects of a wide range of physical processes on the lower trophic levels of the central equatorial Pacific, a relatively simple physical–biological model has been developed. Because of the very high growth rates of the picoplankton and microzooplankton ($O(1 \, d^{-1})$) the biology directly responds to physical forcing on these daily time scales. Therefore, forcing the model directly with environmental data collected via the TAO mooring eliminates many potential problems that can arise in ecosystem models forced by flow fields derived from numerical circulation models.

Simulated time series reproduce much of the variability in phytoplankton chlorophyll, zooplankton biomass, ammonium concentration, nitrate concentration, rate of primary production, *f*-ratio, phytoplankton growth rate, and zooplankton grazing rate observed during the EqPac cruises. Idealized modeling experiments isolate the effects of various environmental forcing factors on the equatorial Pacific ecosystem over a wide range of time scales. Results suggest that the deeper thermocline associated with the 1991–92 El Niño is responsible for the lower productivities observed during TS1 as compared to TS2, and that changes in species composition were not required to reproduce this variability in the rate of primary productivity. Because of the strong coupling between the fast-growing picoplankton and their equally fast-growing microzooplankton predators, the zooplankton are able to keep up with increased rates of primary production, and simulated phytoplankton chlorophyll therefore remains constant on these time scales. This result is inconsistent with cruise observations which show significantly lower chlorophyll levels during TS1; the simulations suggest that these decreased concentrations must be due to higher frequency processes, rather than due to El Niño-related changes in thermocline depth.

Tropical instability waves provide a primary source of physical variability in the equatorial Pacific Ocean, and are characterized by 20-d oscillations in meridional and vertical velocity. Strong northward velocities resulting from these waves appear to be temporally associated with periods of high chlorophyll concentration (Fig. 11) and high diatom abundance (Iriarte and Fryxell, 1995; Bidigare and Ondrusek, 1996) as well as with strong downwelling velocities (Figs. 7A and B; Weisberg and Qiao, 2000). This is consistent with the results of previous studies (Flament et al., 1996; Johnson et al., 1996; Archer et al., 1997), which show that a strong convergent front oriented from northeast to southwest is typically located at the western (leading) edge of each TIW, separating the northward-flowing cold nutrient-rich water in the south from the southeastward-flowing warm nutrient-poor water to the north. The fact that the high abundance of diatoms is associated with downwelling velocities suggests that the increase in diatom abundance cannot be explained solely by an increase in the concentration of iron. On the contrary, this increase in diatom abundance appears to result from both the in situ growth of diatoms in the localized upwelling region associated with the TIW, as well as the horizontal advection of diatoms into the convergence/downwelling region.

Equatorially trapped internal gravity waves are a ubiquitous feature of the central equatorial Pacific, and one that may have been undersampled by the JGOFS EqPac cruises. Simulation results suggest that these waves dominate variability in primary production and biomass fields. By advecting iron-enriched, low-chlorophyll water up into the euphotic zone, IGWs can cause both in situ growth in the upper water column, as well as phytoplankton-dilution effects near the base of the euphotic zone. Because iron uptake rates of picoplankton are high compared to the frequency of these waves, IGWs may provide a large flux of iron into the euphotic zone. If these internal gravity waves are not included in the physical model, such as when ecosystem models are forced by numerical circulation model output, iron flux may be significantly underestimated and the net effect of these waves will need to be parameterized.

The simulated and observed results discussed here clearly show the need to model and sample at time and space scales at which environmental and biological frequencies match. Thus, future multidisciplinary oceanographic programs need to be designed from the outset to ensure that appropriate matching of frequencies occurs. Without this, attempts to relate cause and effect and to define mechanisms underlying observed biological–physical interactions, will be compromised.

Appendix A. Vertical velocity

Total vertical velocity (w) can be written as

$$w = w_C + w_A, \tag{A.1}$$

where w_C and w_A are the cross- and along-isothermal components of vertical velocity, respectively. The scaling of each of these terms is described below.

A.1. Scaling of w_C

Bryden and Brady (1985) used a diagnostic model to determine that in the upper 200 m between 150°W and 110°W in the equatorial Pacific, cross-isothermal velocities are substantially smaller than their along-isothermal counterparts on annual time scales. For instance, between 100 and 140 m where nutrient gradients are typically quite large, and thus where the accuracy of w matters most for the vertical advection term, cross-isothermal velocities are less than 5% of total vertical velocity (Bryden and Brady, 1985). In a related analysis, Weisberg and Qiao (2000) used data from an array of acoustic Doppler current profilers to estimate horizontal divergence and vertical velocity at 0°N, 140°W. Results of this analysis also suggest that between 50 and 120 m, cross-isothermal vertical velocities are small compared to along-isothermal vertical velocities on annual time scales (see Figs. 10 and 11 of Weisberg and Qiao, 2000).

Unfortunately, it is more difficult to assess the relative magnitudes of cross- and along-isothermal vertical velocities on daily time scales. Instantaneous along-isothermal velocities can exceed $15\,\mathrm{m\,d^{-1}}$ (Harrison, 1996; Weisberg and Qiao, 2000), but data on instantaneous cross-isothermal velocities are not available. Model results are of little help in clarifying this issue, since fully three-dimensional circulation models are often very dependent upon the specific turbulence parameterization used (Weisberg and Qiao, 2000). A simple scaling analysis, however, can be used to demonstrate that cross-isothermal vertical velocities may be negligible as compared to along-isothermal vertical velocities on daily time scales. The two diapycnal processes controlling temperature are (i) heating by penetrating solar radiation and (ii) small-scale vertical mixing associated with a diapycnal velocity (w_C) (Gouriou and Reverdin, 1992). Because the vertical gradients of the biological and chemical quantities of interest are highest in the lower euphotic zone, this is where the effects of incorrectly computing vertical velocity will be most profound. Since

the effects of penetrating solar radiation are small in the lower euphotic zone, the one-dimensional equation governing the temperature (T) distribution in a reference frame following a vertically moving isotherm, is

$$w_C \frac{\partial T}{\partial z} \approx K_z \frac{\partial^2 T}{\partial z^2}.$$

In this formulation K_z is the vertical eddy diffusivity coefficient, double diffusive effects are assumed to be small, and salinity variations are neglected. This relationship can be used to scale w_C as follows:

$$w_C \approx \frac{K_z}{H} \approx \frac{10^{-4} \, m^2 \, s^{-1}}{100 \, m} \approx 0.1 \, m \, d^{-1},$$

where the vertical depth scale, H, is assumed to be the depth of the euphotic zone. Since instantaneous along-isothermal velocities range from 2 to $20 \, m \, d^{-1}$ (Harrison, 1996; Weisberg and Qiao, 2000) this scaling analysis further supports the assumption that $w_C \ll w_A$ on daily time scales.

A.2. Scaling of w_A

The along-isothermal component of vertical velocity is due to two effects: (i) local upward movement of the isotherm ($\partial\eta/\partial t$) and (ii) advection along a stationary, sloping isotherm ($\mathbf{u} \cdot \nabla\eta$):

$$w_A = \frac{\partial\eta}{\partial t} + \mathbf{u} \cdot \nabla\eta. \tag{A.2}$$

In this region where the thermocline tilts upward to the east but is relatively flat within several degrees to the north and south, the meridional component of along-isothermal velocity is negligible as compared to the zonal component, i.e. $\mathbf{u} \cdot \nabla\eta \approx u \, \partial\eta/\partial x$.

On daily/weekly time scales, the ratio of $u\partial\eta/\partial x$ to $\partial\eta/\partial t$ is equivalent to the ratio of u to c, where u is the particle velocity and c is the horizontal phase speed associated with the equatorially trapped internal gravity waves that have periods of 6–8 d. If the phase speed of these waves is of order $(g'H)^{1/2}$, where g' is reduced gravity ($0.01 \, m^2 \, s^{-1}$) and H is the depth of the thermocline (100 m), then $c = 1 \, m \, s^{-1}$. The TAO current meter mooring can be used to estimate that the particle velocity associated with these waves is on the order of $0.1 \, m \, s^{-1}$ or less, again indicating that $u \ll c$ and similarly $u\partial\eta/\partial x \ll \partial\eta/\partial t$ by at least an order of magnitude.

Data from the 140°W TAO mooring sensors support the scaling analysis presented above. These data indicate that on daily time scales the isotherms in the euphotic zone make large vertical excursions, at times exceeding $20 \, m \, d^{-1}$. At 50 m depth the average value of $|\partial\eta/\partial t|$ is on the order of $0.0001 \, m \, s^{-1}$. Current meter data from this mooring show that the mean zonal velocity at 50 m is about $0.5 \, m \, s^{-1}$; however, estimates of the magnitude of $\partial\eta/\partial x$ are difficult to obtain from TAO data. Given the above information, the instantaneous zonal isotherm slope would have to be equivalent to a 40 m rise over a distance of 100 km in order for $u\partial\eta/\partial x \approx \partial\eta/\partial t$. It is difficult to

estimate instantaneous zonal isotherm slopes over such small distances (O(100 km)), since moorings are typically spaced at intervals that exceed this distance. Therefore, estimates of these isotherm slopes are best computed from in situ cruise data. Zonal isotherm slopes can be estimated from the Zonal Flux cruise hydrographic data, which indicate that isotherms rise 40 m over a zonal distance of 5° longitude near 150°W (LeBorgne et al., 1999). Although these data are not precisely synoptic, they do suggest that on short time scales $u\partial\eta/\partial x \ll \partial\eta/\partial t$.

On longer (monthly/annual) time scales, the time rate of change component of vertical velocity ($\partial\eta/\partial t$) averages to zero, i.e. over the long term, isotherms neither rise out of the surface of the ocean nor sink to the bottom. On these time scales, however, total vertical velocity is not zero. An important feature of the steady-state equatorial circulation pattern includes a background level of equatorial upwelling with magnitude $O(u\partial\eta/\partial x)$. An estimate of this background level of upwelling can be obtained by multiplying the mean zonal velocity ($0.5\,\mathrm{m\,s^{-1}}$) by the mean zonal isotherm slope at 140°W (40 m over 5–15° longitude) to obtain a 1–$3\,\mathrm{m\,d^{-1}}$ vertical velocity. This estimate is consistent with most other estimates of annual averaged vertical velocity in this region (Bryden and Brady, 1985; Weisberg and Qiao, 2000).

Therefore, on daily time scales $w_A \approx \partial\eta/\partial t$, whereas when annual averages are computed, $w_A \approx u\partial\eta/\partial x$. Because this analysis deals both with short time scales (IGWs with 6–8 d periods) and relatively long time scales (interannual El Niño forcing), both components, i.e. $u\partial\eta/\partial x$ and $\partial\eta/\partial t$, must be included in the computation of vertical velocity.

A.3. Vertical velocity computation

Daily estimates of $\partial\eta/\partial t$ can be obtained by evaluating the change in the depths of the isotherms measured by the TAO temperature sensors at 140°W. In the upper 50 m where mixing and heating may result in significant cross-isothermal velocities, vertical velocity is assumed to decrease linearly to a value of zero at the surface. The remaining component of w, i.e $u\partial\eta/\partial x$, is computed by multiplying zonal velocity data at 140°W by estimates of zonal isotherm slopes. Isothermal slopes can be obtained using subsurface temperature time series at specified depths from the TAO moorings at 155°W, 140°W, and 125°W. These time series were averaged over 30 d, based on the time it would take for a particle in the Equatorial Undercurrent to traverse the distance between 155°W and 125°W at an average speed of $0.12\,\mathrm{m\,s^{-1}}$. Zonal isotherm slopes between 40 and 140 m are computed from the averaged data at 155°W and 125°W, unless the isotherm outcrops or drops below 180 m in which case data from the 140°W mooring must be substituted. Consistent with the scaling analysis described above, this analysis suggests that although on daily time scales the magnitude of $\partial\eta/\partial t$ exceeds $u\partial\eta/\partial x$ on average by at least an order of magnitude, annually averaged values of $u\partial\eta/\partial x$ are significantly greater than those of $\partial\eta/\partial t$.

A possible source of error in the above calculation of vertical velocity lies in the fact that instantaneous (daily) estimates of $\partial\eta/\partial t$ at 140°W are combined with estimates of $u\partial\eta/\partial x$ derived using monthly averaged data over relatively large spatial scales. However, as discussed above, both the scaling analysis and velocity computations suggest that on daily time scales $\partial\eta/\partial t \gg u\,\partial\eta/\partial x$, and therefore the large spatial and temporal time scales used in computing $u\partial\eta/\partial x$ introduce negligible error into the calculation. On longer time scales the large spatial separation of the moorings is also not expected to be a problem, since hydrographic data from the Zonal Flux cruise (from 165°E to 150°W) show temperature isotherms sloping smoothly and uniformly along

these $25°$ of longitude (LeBorgne et al., 1999). The temporal (30 d) averaging is also not likely to have a significant effect on the vertical velocity computations, since the Kelvin waves that are most prominent in the TAO time-series data have periods of roughly 60–90 d (McPhaden et al., 1998).

Appendix B. Attenuation of light within seawater

In the central equatorial Pacific, where iron limitation typically dominates over light limitation in controlling phytoplankton production, a complex spectral light model is not warranted, yet assuming a constant light attenuation coefficient is inadequate. Therefore, the concept of phytoplankton self-shading, as described by Anderson (1993) is invoked. Anderson (1993) uses a spectral model to derive simple empirical equations for calculating spectrally averaged values for the vertical attenuation of light within an arbitrary number (n) of discrete depth layers, bounded by surfaces $z = Z_i$. Specifically, the attenuation of light at depth z within the rth layer, $R(z)$, is expressed as

$$R(z) = \exp\left\{\left[\sum_{i=1}^{r-1} k_i(Z_i - Z_{i-1})\right] + k_r(z - Z_{r-1})\right\}. \tag{B.1}$$

Vertical attenuation coefficients for the ith layer (k_i) are determined from a fifth-order ($M = 5$) polynomial fit, relating k_i to the square root of the average pigment in layer i ($C_{chlN}P_i$), by means of the coefficient b (Anderson, 1993; Table 4):

$$k_i = \sum_{m=0}^{M} b_{m,i}(C_{chlN} P_i)^{m/2}, \quad i = [1, n]. \tag{B.2}$$

The conversion between mg chl and mmol N (C_{chlN}) can be estimated by assuming a carbon-to-chlorophyll ratio of $70\,\text{mg C (mg chl)}^{-1}$ (Chavez et al., 1996) and a $C\!:\!N$ Redfield ratio of $6.6\,\text{mmol C (mmol N)}^{-1}$, such that $C_{chlN} = 1.13\,\text{mg chl (mmol N)}^{-1}$. Anderson (1993) determined that using three layers ($Z_0 = 0\,\text{m}, Z_1 = -5\,\text{m}, Z_2 = -23\,\text{m}$) provides an acceptable level of accuracy balanced against the need to minimize computational intensity. Because of the depth-integrated approach used in this analysis, P_i is approximated by $\bar{P}$. This yields euphotic zone depths that are slightly too shallow. Therefore, the coefficient $b_{0,3}$ is decreased by 50% in order to account for the observed chlorophyll depth profile (Fig. 6A) and to reproduce observed euphotic zone depths.

References

Anderson, T.R., 1993. A spectrally averaged model of light penetration and photosynthesis. Limnology and Oceanography 38 (7), 1403–1419.

Archer, D., Aiken, J., Balch, W., Barber, D., Dunne, J., Flament, P., Gardner, W., Garside, C., Goyet, C., Johnson, E., Kirchman, D., McPhaden, M., Newton, J., Peltzer, E., Welling, L., White, J., Yoder, J., 1997. A meeting place of great ocean currents: shipboard observations of a convergent front at 2°N in the Pacific. Deep-Sea Research II 44 (9–10), 1827–1849.

Banse, K., 1990. Does iron really limit phytoplankton production in the offshore subarctic Pacific? Limnology and Oceanography 35 (3), 772–775.

Barber, R.T., 1992. Introduction to the WEC88 cruise: an investigation into why the equator is not greener. Journal of Geophysical Research 97 (C1), 609–610.

Barber, R.T., Chavez, F.P., 1991. Regulation of primary productivity rate in the equatorial Pacific. Limnology and Oceanography 36 (8), 1803–1815.

Barber, R.T., Sanderson, M.P., Lindley, S.T., Chai, F., Newton, J., Trees, C., Foley, D., Chavez, F., 1996. Primary productivity and its regulation in the equatorial Pacific during and following the 1991–1992 El Niño. Deep-Sea Research II 43 (4–6), 933–969.

Behrenfeld, M.J., Bale, A.J., Kolber, Z.S., Aiken, J., Falkowski, P.G., 1996. Confirmation of iron limitation of phytoplankton photosynthesis in the equatorial Pacific Ocean. Nature 383, 508–511.

Bidigare, R.R., Ondrusek, M.E., 1996. Spatial and temporal variability of phytoplankton pigment distributions in the central equatorial Pacific Ocean. Deep-Sea Research II 43 (4–6), 809–833.

Bryden, H.L., Brady, E.C., 1985. Diagnostic model of the three-dimensional circulation in the upper equatorial Pacific. Journal of Physical Oceanography 15 (10), 1255–1273.

Carr, M.-E., Lewis, M.R., Kelley, E., Jones, B., 1995. A physical estimate of new production in the equatorial Pacific along 150°W. Limnology and Oceanography 40 (1), 138–147.

Carr, M.-E., Oakey, N.S., Jones, B., Lewis, M.R., 1992. Hydrographic patterns and vertical mixing in the equatorial Pacific along 150°W. Journal of Geophysical Research 97 (C1), 611–626.

Chai, F., Lindley, S.T., Barber, R.T., 1996. Origin and maintenance of a high nitrate condition in the equatorial Pacific. Deep-Sea Research II 43 (4–6), 1031–1064.

Chavez, F.P., Buck, K.R., Coale, K.H., Martin, J.H., DiTullio, G.R., Welschmeyer, N.A., Jacobson, A.C., Barber, R.T., 1991. Growth rates, grazing, sinking and iron limitation of equatorial Pacific phytoplankton. Limnology and Oceanography 36 (8), 1816–1827.

Chavez, F.P., Buck, K.R., Service, S.K., Newton, J., Barber, R.T., 1996. Phytoplankton variability in the central and eastern tropical Pacific. Deep-Sea Research II 43 (4–6), 835–870.

Coale, K.H., Fitzwater, S.E., Gordon, R.M., Johnson, K.S., Barber, R.T., 1996a. Control of community growth and export production by upwelled iron in the equatorial Pacific Ocean. Nature 379, 621–624.

Coale, K.H., Johnson, K.S., Fitzwater, S.E., Gordon, R.M., Tanner, S., Chavez, F.P., Ferioli, L., Sakamoto, C., Rogers, P., Millero, F., Steinberg, P., Nightingale, P., Cooper, D., Cochlan, W.P., Landry, M.R., Constantinou, J., Rollwagen, G., Trasvina, A., Kudela, R., 1996b. A massive phytoplankton bloom induced by an ecosystem-scale iron fertilization experiment in the equatorial Pacific Ocean. Nature 383, 495–501.

Cullen, J.J., Lewis, M.R., Davis, C.O., Barber, R.T., 1992. Photosynthetic characteristics and estimated growth rates indicate grazing is the proximate control of primary production in the equatorial Pacific. Journal of Geophysical Research 97 (C1), 639–654.

Duce, R.A., Tindale, N.W., 1991. Atmospheric transport of iron and its deposition in the ocean. Limnology and Oceanography 36 (8), 1715–1726.

Dugdale, R.C., Goering, J.J., 1967. Uptake of new and regenerated forms of nitrogen in primary productivity. Limnology and Oceanography 12 (2), 196.

Dunne, J.P., Murray, J.W., Rodier, M., Hansell, D.A., 2000. Export flux in the western and central equatorial Pacific: zonal and temporal variability. Deep-Sea Research I 47 (5), 901–9361.

Fasham, M.J.R., Sarmiento, J.L., Slater, R.D., Ducklow, H.W., Williams, R., 1993. Ecosystem behavior at Bermuda Station "S" and Ocean Weather Station "India": a general circulation model and observational analysis. Global Biogeochemical Cycles 7 (2), 379–415.

Fitzwater, S.E., Coale, K.H., Gordon, R.M., Johnson, K.S., Ondrusek, M.E., 1996. Iron deficiency and phytoplankton growth in the equatorial Pacific. Deep-Sea Research II 43 (4–6), 995–1015.

Flament, P.J., Kennan, S.C., Knox, R.A., Niiler, P.P., Bernstein, R.L., 1996. The three-dimensional structure of an upper ocean vortex in the tropical Pacific Ocean. Nature 383, 610–613.

Foley, D.G., Dickey, T.D., McPhaden, M.J., Bidigare, R.R., Lewis, M.R., Barber, R.T., Lindley, S.T., Garside, C., Manov, D.V., McNeil, J.D., 1997. Longwaves and primary productivity variations in the equatorial Pacific at, 0° and 140°W. Deep-Sea Research II 44 (9–10), 1801–1826.

Franks, P.J.S., Wroblewski, J.S., Flierl, G.R., 1986. Behavior of a simple plankton model with food-level acclimation by herbivores. Marine Biology 91, 121–129.

Frost, B.W., 1996. Phytoplankton bloom on iron rations. Nature 383, 475–476.

Frost, B.W., Franzen, N.C., 1992. Grazing and iron limitation in the control of phytoplankton stock and nutrient concentration: a chemostat analogue of the Pacific equatorial upwelling zone. Marine Ecology Progress Series 83, 291–303.

Frouin, R., Lingner, D.W., Gautier, C., Baker, K.S., Smith, R.C., 1989. A simple analytical formula to compute clear sky total and photosynthetically available solar irradiance at the ocean surface. Journal of Geophysical Research 94 (C7), 9731–9742.

Gordon, R.M., Coale, K.H., Johnson, K.S., 1997. Iron distributions in the equatorial Pacific: Implications for new production. Limnology and Oceanography 42 (3), 419–431.

Gouriou, Y., Reverdin, G., 1992. Isopycnal and diapycnal circulation of the upper equatorial Atlantic Ocean in 1983-1984. Journal of Geophysical Research 97 (C3), 3543–3572.

Greene, R.M., Geider, R.J., Falkowski, P.G., 1991. Effect of iron limitation on photosynthesis in a marine diatom. Limnology and Oceanography 36 (8), 1772–1782.

Gregg, W.W., Carder, K.L., 1990. A simple spectral solar irradiance model for cloudless maritime atmospheres. Limnology and Oceanography 35 (8), 1657–1675.

Halpern, D.R., Knox, R.A., Luther, D.S., 1988. Observations of 20-day period meridional current oscillations in the upper ocean along the Pacific equator. Journal of Physical Oceanography 18 (11), 1514–1534.

Hansen, D.V., Swenson, M.S., 1996. Mixed layer circulation during EqPac and some thermochemical implications for the equatorial cold tongue. Deep-Sea Research II 43 (4–6), 707–724.

Harrison, D.E., 1996. Vertical velocity in the central tropical Pacific: a circulation model perspective for JGOFS. Deep-Sea Research II 43 (4–6), 687–705.

Hayes, S.P., Mangum, L.J., Picaut, J., Sumi, A., Takeuchi, K., 1991. TOGA/TAO: a moored array for real-time measurements in the tropical Pacific Ocean. Bulletin of the American Meteorological Society 72 (3), 339–347.

Hofmann, E.E., Ambler, J.W., 1988. Plankton dynamics on the outer southeastern U.S. continental shelf. Part II: a time-dependent biological model. Journal of Marine Research 46 (4), 883–917.

Hurtt, G.C., Armstrong, R.A., 1999. A pelagic ecosystem model calibrated with BATS and OWS I data. Deep-Sea Research I 46 (1), 27–61.

Iriarte, J.L., Fryxell, G.A., 1995. Micro-phytoplankton at the equatorial Pacific (140°W) during the JGOFS EqPac Time Series studies: March to April and October 1992. Deep-Sea Research II 42 (2–3), 559–583.

Ivlev, V.S., 1955. Experimental Ecology of the Feeding of Fishes. Pischepromizdat, Moscow, 302pp. (Translated from Russian by D. Scott. Yale University Press, New Haven, 1961).

Johnson, E.S., 1996. A convergent instability wave front in the central tropical Pacific. Deep-Sea Research II 43 (4–6), 753–778.

Kessler, W.S., McPhaden, M.J., 1995. The 1991–1993 El Niño in the central Pacific. Deep-Sea Research II 42 (2–3), 295–333.

Klein, P., Steele, J.H., 1985. Some physical factors affecting ecosystems. Journal of Marine Research 43 (2), 337–350.

Landry, M.R., Barber, R.T., Bidigare, R.R., Chai, F., Coale, K.H., Dam, H.G., Lewis, M.R., Lindley, S.T., McCarthy, J.J., Roman, M.R., Stoecker, D.K., Verity, P.G., White, J.R., 1997. Iron and grazing constraints on primary production in the central equatorial Pacific: an EqPac synthesis. Limnology and Oceanography 42 (3), 405–418.

Landry, M.R., Constantinou, J., Kirshtein, J., 1995. Microzooplankton grazing in the central equatorial Pacific during February and August, 1992. Deep-Sea Research II 42 (2–3), 657–671.

Le Borgne, R., Rodier, M., Le Bouteiller, A., Murray, J.W., 1999. Zonal variability of plankton and particle export flux in the equatorial Pacific upwelling between 165°E and 150°W. Oceanologica Acta 22 (1), 57–66.

Legeckis, R., 1977. Long waves in the eastern equatorial Pacific ocean: a view from a geostationary satellite. Science 197, 1179–1181.

Leonard, C.L., McClain, C.R., Murtugudde, R., Hofmann, E.E., Harding, L.W., 1999. An iron-based ecosystem model of the central equatorial Pacific. Journal of Geophysical Research 104 (C1), 1325–1341.

Lien, R.-C., Caldwell, D.R., Gregg, M.C., Moum, J.N., 1995. Turbulence variability at the equator in the central Pacific at the beginning of the 1991–1993 El Niño. Journal of Geophysical Research 100 (C4), 6881–6898.

Lindley, S.T., Bidigare, R.R., Barber, R.T., 1995. Phytoplankton photosynthesis parameters along 140°W in the equatorial Pacific. Deep-Sea Research II 42 (2–3), 441–463.

Loukos, H., Frost, B., Harrison, D.E., Murray, J.W., 1997. Ecosystem model with iron limitation of primary production in the equatorial Pacific at 140°W. Deep-Sea Research II 44 (9–10), 2221–2249.

Martin, J.H., Broenkow, W.W., Fitzwater, S.E., Gordon, R.M., 1990. Yes it does: a reply to the comment by Banse. Limnology and Oceanography 35 (3), 775–777.

Martin, J.H., Coale, K.H., Johnson, K.S., Fitzwater, S.E., Gordon, R.M., Tanner, S.J., Hunter, C.N., Elrod, V.A., Nowicki, J., Coley, T.L., Barber, R.T., Lindley, S., Watson, A.J., Van Scoy, K., Law, C.S., Liddicoat, M.I., Ling, R., Stanton, T., Stockel, J., Collins, C., Anderson, A., Bidigare, R., Ondrusek, M., Latasa, M., Millero, F.J., Lee, K., Yao, W., Zhang, J.Z., Friederich, G., Sakamoto, C., Chavez, F., Buck, K., Kolber, Z., Greene, R., Falkowski, P., Chishom, S.W., Hoge, F., Swift, R., Yungel, J., Turner, S., Nightingale, P., Hatton, A., Liss, P., Tindale, N.W., 1994. Testing the iron hypothesis in ecosystems of the equatorial Pacific Ocean. Nature 371, 123–129.

Martin, J.H., Fitzwater, S.E., 1988. Iron deficiency limits phytoplankton growth in the North-East Pacific subarctic. Nature 331, 341–343.

Martin, J.H., Gordon, R.M., Fitzwater, S.E., Broenkow, W.W., 1989. VERTEX: phytoplankton/iron studies in the Gulf of Alaska. Deep-Sea Research 36 (5), 649–680.

McCarthy, J.J., Garside, C., Nevins, J.L., Barber, R.T., 1996. New production along 140°W in the equatorial Pacific during and following the 1992 El Niño event. Deep-Sea Research II 43 (4–6), 1065–1093.

McGillicuddy Jr., D.J., Johnson, R., Siegel, D.A., Michaels, A.F., Bates, N.R., Knap, A.H., 1999. Mesoscale variations of biogeochemical properties in the Sargasso Sea. Journal of Geophysical Research 104 (C6), 13381–13394.

McPhaden, M.J., 1993. TOGA-TAO and the 1991–93 El Niño-Southern Oscillation event. Oceanography 6 (2), 36–44.

McPhaden, M.J., Busalacchi, A.J., Cheney, R., Donguy, J.-R., Gage, K.S., Halpern, D., Ji, M., Julian, P., Meyers, G., Mitchum, G.T., Niiler, P.P., Picaut, J., Reynolds, R.W., Smith, N., Takeuchi, K., 1998. The Tropical Ocean Global Atmosphere (TOGA) observing system: a decade of progress. Journal of Geophysical Research 103 (C7), 14169–14240.

Morel, A., 1988. Optical modeling of the upper ocean in relation to its biogenous matter content (Case 1 waters). Journal of Geophysical Research 93 (C9), 10749–10768.

Morel, F.M.M., Rueter, J.G., Price, N.M., 1991. Iron nutrition of phytoplankton and its possible importance in the ecology of ocean regions with high nutrient and low biomass. Oceanography 4 (2), 56–61.

Murray, J., Leinen, M.W., Feely, R.A., Toggweiler, J.R., Wanninkhof, R., 1992. Eqpac: a process study in the central equatorial Pacific. Oceanography 5 (3), 134–142.

Murray, J.W., Barber, R.T., Roman, M.R., Bacon, M.P., Feely, R.A., 1994. Physical and biological controls on carbon cycling in the equatorial Pacific. Science 266, 58–65.

Murray, J.W., Johnson, E., Garside, C., 1995. A U.S. JGOFS process study in the equatorial Pacific (EqPac): introduction. Deep-Sea Research II 42 (2–3), 275–293.

Perigaud, C., 1990. Sea level oscillations observed with Geosat along the two shear fronts of the Pacific North Equatorial Countercurrent. Journal of Geophysical Research 95 (C5), 7239–7248.

Platt, T., Gallegos, C.L., Harrison, W.G., 1980. Photoinhibition of photosynthesis in natural assemblages of marine phytoplankton. Journal of Marine Research 38 (4), 687–701.

Price, N.M., Ahner, B.A., Morel, F.M.M., 1994. The equatorial Pacific Ocean: grazer-controlled phytoplankton populations in an iron-limited ecosystem. Limnology and Oceanography 39 (3), 520–534.

Price, N.M., Anderson, L.F., Morel, F.M.M., 1991. Iron and nitrogen nutrition of equatorial Pacific plankton. Deep-Sea Research 38 (11), 1361–1378.

Qiao, L., Weisberg, R.H., 1995. Tropical instability wave kinematics: observations from the Tropical Instability Wave Experiment. Journal of Geophysical Research 100 (C5), 8677–8693.

Roman, M.R., Dam, H.G., Gauzens, A.L., Urban-Rich, J., Foley, D.G., Dickey, T.D., 1995. Zooplankton variability on the equator at 140°W during the JGOFS EqPac study. Deep-Sea Research II 42 (2–3), 673–693.

Siegel, D.A., McGillicuddy Jr., D.J., Fields, E.A., 1999. Mesoscale eddies, satellite altimetry and new production in the Sargasso Sea. Journal of Geophysical Research 104 (C6), 13359–13379.

Steele, J.H., Frost, B.W., 1977. The structure of plankton communities. Philosophical Transactions of the Royal Society of London 280 (976), 485–534.

Timmermans, K.R., Stolte, W., De Baar, H.J.W., 1994. Iron-mediated effects on nitrate reductase in marine phyto-plankton. Marine Biology 121, 389–396.

Verity, P.G., Stoecker, D.K., Sieracki, M.E., Nelson, J.R., 1996. Microzooplankton grazing of primary production in the equatorial Pacific. Deep-Sea Research II 43 (4–6), 1227–1256.

Walsh, I.D., Chung, S.P., Richardson, M.J., Gardner, W.D., 1995. The diel cycle in the integrated particle load in the equatorial Pacific: a comparison with primary production. Deep-Sea Research II 42 (2–3), 465–477.

Weisberg, R.H., Qiao, L., 2000. Equatorial upwelling in the central Pacific estimated from moored velocity profilers. Journal of Physical Oceanography 30 (1), 105–124.

White, J.R., Zhang, X., Welling, L.A., Roman, M.R., Dam, H.G., 1995. Latitudinal gradients in zooplankton biomass in the tropical Pacific at 140°W during the JGOFS EqPac study: effects of El Niño. Deep-Sea Research II 42 (2–3), 715–733.

Wunsch, C., Gill, A.E., 1976. Observations of equatorially trapped waves in Pacific sea level variations. Deep-Sea Research 23 (5), 371–390.

Yu, A., McCreary, J.J.P., Proehl, J.A., 1995. Meridional asymmetry and energetics of tropical instability waves. Journal of Physical Oceanography 25 (12), 2997–3007.

Yoder, J.A., Ackleson, S.G., Barber, R.T., Flament, P., Balch, W.M., 1994. A line in the sea. Nature 371, 689–692.

Zettler, E.R., Olson, R.J., Binder, B.J., Chisholm, S.W., Fitzwater, S.E., Gordon, R.M., 1996. Iron-enrichment bottle experiments in the equatorial Pacific: responses of individual phytoplankton cells. Deep-Sea Research II 43 (4–6), 1017–1029.